TECHNICAL PAPER

Signal-based parameter and fault identification in roller bearings using adaptive neuro-fuzzy inference systems

Rajasekhara Reddy Mutra[1] · D. Mallikarjuna Reddy[1] · J. Srinivas[2] · D. Sachin[1] · K. Babu Rao[3]

Abstract

The rolling element bearings are used in high load-bearing, high stiffness, and high-speed applications. They have wide applications in aero-engine and automobile rotors. In practice, major rotor failures occur with bearing faults. Therefore, it is required to identify the location and intensity of such bearing faults from time to time. In recent times, several signal-based fault identification approaches were proposed for the condition monitoring of ball and roller bearing systems in rotors. In the present work, an experimental framework of the rotor-bearing system is established to study the dynamics of the system under different operating conditions including the faults on the inner race, roller, and outer race. Experiments are conducted under different operating conditions with these faults. The experimental results are compared initially with finite element analysis as a means of validation. Using the empirical mode decomposition (EMD) method, the intrinsic modal functions are estimated for the time response signals. An inverse identification approach is proposed for the identification of the operating parameters from the vibration response using a counter propagation neural network (CPNN) model. Later, an adaptive neuro-fuzzy inference system (ANFIS) is proposed for the classification and identification of faults by analyzing the operating conditions from CPNN and statistical parameters from EMD. The proposed CPNN- and ANFIS-based methodology could predict the faults in roller by 100%, inner race by 87.5%, and outer race by 96%.

Keywords Fault detection · Empirical mode decomposition · Feature extraction · Soft computing schemes

Technical Editor: Jarir Mahfoud.

✉ Rajasekhara Reddy Mutra
  rajmech03@gmail.com

  D. Mallikarjuna Reddy
  dmreddy@vit.ac.in

  J. Srinivas
  srin07@yahoo.co.in

  D. Sachin
  7.Sachind@gmail.com

  K. Babu Rao
  babusan1401@gmail.com

[1] Dynamics and Vibration Lab, School of Mechanical Engineering, Vellore Institute of Technology, Vellore, Tamil Nadu 632014, India

[2] Department of Mechanical Engineering, National Institute of Technology, Rourkela, Odisha 769008, India

[3] Department of Design & Automation, School of Mechanical Engineering, Vellore Institute of Technology, Vellore, Tamil Nadu 632014, India

1 Introduction

Machinery health monitoring is gaining more importance in the industry because of the need to improve reliability and reduce the risk of production loss due to machinery breakdowns. The use of acoustic and vibration signals is common in the domain of condition monitoring of both structures and rotating machinery. By comparing the vibration or acoustic signals of a machine running in healthy or normal and faulty conditions, identification of faults like rotor rub, unbalance of mass, failure of gears, misalignment of the shaft, and bearing faults is possible. These signal data can also be used to identify the incipient failures of the machinery components, using the online monitoring system, decreasing the prospect of catastrophic failure and downtime. For the detection of machinery-bearing faults, a variety of modern signal processing approaches are available. These approaches are utilized to examine bearing defect signal data utilizing time domain [1–3], frequency domain [4–7], and a combination of the two time–frequency-domain methods [8]. These approaches each have their own set of benefits

and drawbacks. The presence of noise can distort fault data recorded in the form of vibration or acoustic signals for bearing problems. To detect early onset failures, a suitable signal processing approach is required [9, 10]. Tang et al. [11] explained the spatial localization of acoustic technique to identify the defect localization on rolling element bearing stationary outer race. Maczak and Jasinski [12] investigated local faults in gears using a model-based approach. Inturi et al. [13] described the experimental analysis of the three-stage gearbox under constant and fluctuating operating conditions with bearing faults using wavelet transform to predict the different statistical parameters. Further, based on the fault severity the identified fault is classified using a support vector machine. In continuation to this, the support vector machine is used to extract the features from a rotor vibration signal and acoustic emission to classify the misalignment presented in the paper [14]. The advantage of this method was the direct use of the time signal processing algorithms for the implementation of the diagnostic systems working online simply and faster.

Vibration-based analysis has been increasingly popular for diagnosing bearing faults in recent years. The rotating machine's characteristics are reflected in the vibration data, which is based on the premise that all elements of the system influence the vibration signal. As a result, analyzing vibration signal data is critical for ensuring that the equipment runs without failure. Unfortunately, these methods are not able to provide inherent data related to non-stationary signals. These methods give only a partial performance for machinery diagnostics. To overcome this problem, a signal processing technique called Wavelet analysis also called the time–frequency method has been introduced. The wavelet transform method is a variable window method, which uses a time-domain signal interval to find out the respective frequency components of the same signal. When compared to a raw vibration signal, it has been proven in recent years that the statistical measure of kurtosis detects the fault at an early stage. A value of kurtosis > 3 indicates the presence of defects [15]. In the identification and estimation of faults, the wavelet transform technique [16, 17] has been widely employed. The non-stationary signal is analyzed using the wavelet technique. The fixed window size in wavelet analysis is a drawback. A high-frequency component may be detected effectively in advance (with less relative error) than a low-frequency component by modifying the window size, and a low-frequency component can be identified well in comparison to a high-frequency component by adjusting the window size. In many cases, the wavelet method is used in combination with additional features, such as Gaussian/ exponential enveloped functions and support vector regressions [18, 19]. Tabrizi et al. [20] identified the small defects in the roller bearings by using the wavelet packet decomposition (WPD) and empirical mode decomposition (EMD) methods.

De-noising techniques [21] are used to enrich the fault detection process. The wavelet packet transform method (WPT) is a simplification of the wavelet transform method and has been used in many signal processing applications such as de-noising and compression [22–24]. Spectral Kurtosis analysis and combined ensemble empirical mode decomposition (EEMD) is used for fault identification of rolling bearing [25]. The method of empirical mode decomposition (EMD) along with Hilbert–Huang transform (HHT) is used to obtain the features data of bearing defect signal, which can understand the condition monitoring of fault signal [26]. Li et al. [27] demonstrated twelve sensitive features of bearing fault signals for early fault identification. Both empirical mode decomposition and wavelet packet analysis are together used to get the features and are then given as inputs for Radial Basis Function Networks (RBFNs) to categorize different faults [28]. In the work, three different types of neural network models were used for fault analysis of bearing elements. The effectiveness of fault detection in the bearings using the deep neural network (DNN) technique and convolution neural network over ANN was studied [29–31] successfully and demonstrated the intelligent fault detection method of rotating machinery with huge test data. This study also highlighted the advantages of using deep neural networks over shallow networks. The same method was validated using data captured from the bearing and gearbox. Mutra et al. [32, 33] used a neural network-based surrogate model to explain the parametric identification of a high-speed rotor system supported on oil/oil-free bearings. An impulse is created whenever a rolling element passes through a local fault in a bearing. Because the impulse period is so short in comparison to the time between pulses, the induced energy will be spread out across a large frequency range. As a result, the impact pressures will excite numerous resonances of the bearing and the entire structure, and the FFT technique will be unable to determine the problem frequencies. Envelope detection is a technique for converting a bipolar input signal to a unipolar signal using a smoothing circuit for FFT analysis of system frequencies. [34]. Zhou et al. [35] demonstrated the identification of the fault characteristics of the motor base screw loosening through online vibration by using the similarity measurement theory. The corresponding amplitude and frequency characteristics of the curve were obtained from the FFT technique. Cai et al. [36] explained a new method for fault diagnosis for rolling bearings by combining the instantaneous spectrum estimation with fractional Fourier instantaneous spectrum (FRFT). Here the maximum kurtosis coefficient method is used to estimate the spectrum of the optimal fractional domain. Moshrefzadeh and Fasana [37] explained the lumped parameter model to identify the frequency response of the planetary gearbox with different faults in the bearings. Ho and Randall [38] proposed a method of

envelope analysis using the Hilbert–Huang transform. Hilbert transform is applied in frequency bands where the signal-to-noise ratio is maximum. Rai and Mohanty [39] demonstrated bearing fault detection using Hilbert–Huang transform (HHT) method to capture characteristic defect frequencies of a rotating bearing. HHT provides multi-resolution in various frequency scales as it takes signal frequency with its variation in the time domain for consideration. However, it has an error in the estimation of defect frequencies of the bearings. To enhance the resolution of the Hilbert transforming frequency domain, the researchers used FFT of intrinsic mode functions (IMFs). Mutra and Srinivas [40] explained the identification of floating ring bearing coefficients from the vibration response using a modified particle swarm optimization scheme. Ali et al. [41] employed a soft computing method for both empirical mode decomposition and the artificial neural network (ANN) technique in automatic fault detection and Diagnosis (FDD) of bearings elements using vibration data is proposed. Presently, artificial neural networks [42, 43] have gained more attention in industrial automation applications. Also, a neural network is used for data processing and classification technique. Correspondingly, an artificial intelligence self-adaptive FDD system inspired by the genetic algorithm (GA) and nearest neighbor (NN) was studied in [44]. Literature studies show that online and automated monitoring can be achieved by incorporating the expert systems such as ANN Support Vector Machine (SVM) and k-nearest neighbor to detect faults in the machine. Even though roller bearing identification is not new, the proposed methodology simplifies the approach with the use of experimental data. The reliability and speed of identification are the main targets in the present work. Because of the high efficiency to identify similarities among large data matrices, ANN has gained popularity over its competitors. For hyperspectral image classification, a feature extraction method integrating principal component analysis and local binary pattern is presented in [45]. Vibration amplitude feature extraction from spectral imaging Convolution Deep Believe Network (CDBN) is proposed in [46]. To learn the extracted features CDBN along with Gaussian distribution is utilized. To minimize the sum of the economic cost and maximize customer satisfaction, a time-dependent split delivery green vehicle routing problem with multiple time windows is presented in [47]. To accelerate the convergence, a dynamic parameter adjustment mechanism by particle swarm optimization and the fuzzy is developed in [48]. To solve the large-scale traveling salesman problems the proposed method worked satisfactorily. Adaptive mathematical morphology spectrum [49] used in scale selection methods that depends on experimental parameters like noise ratio, fault frequencies, etc.

Despite all the above fault identification research, there are limited works that make use of experimental data directly to predict the fault locations in rotor-bearing systems accurately. The current research focuses on dynamic modeling and experimental research of a rotor-bearing system with common bearing defects. Extraction of fault features using the EMD method is developed and neural network model is employed to predict the parameters and an Adaptive Fuzzy-Neuro inference system is used to identify the bearing fault type. The contribution of this paper mainly includes (i) a multi-stage-prediction model for fault identification in roller bearings from non-stationary time series. (ii) Demonstrated prediction accuracy of various parameters using statistical features. (iii) Illustrated the efficiency of the proposed model to predict different types of fault types. (iv) A finite element model is developed to simulate fault signals in roller bearings. (v) Post-processing of time series data using statistical parameters is presented. (vi) Inverse model is developed to identify the operating parameters from the vibration response and the fault classification using ANFIS is the prime novelty in this paper.

The following is how the rest of the article is organized:

The mathematical model of the rotor-bearing system is described in Sect. 2. The architecture of a suggested system is discussed in Sect. 3. Section 4 explains the experimentation performed to collect the vibration data of bearings at various runtimes and the empirical mode decomposition (EMD) method, which results in the feature extraction and selection procedure. Section 5 presents the conclusion drawn with the future direction.

2 Mathematical modeling of the rotor-bearing system

The rotor model is simplified using the finite element (FE) method as shown in Fig. 1, with four degrees of freedom per node, which are two bending deflections (U_x, U_y) and their corresponding slopes (θ_x, θ_y).

The rotor system's equations of motion are as follows:

$$[M]\{\ddot{q}\} + ([C] - \omega[G])\{\dot{q}\} + [K]\{q\} = \{F_B\} \tag{1}$$

where $[M]$, $[C]$, $[K]$ are the effective mass, damping, and square stiffness matrices, and $[G]$ is a skew-symmetric gyroscopic matrix, ω is rotational speed while $\{q\}$ is a vector representing displacements.
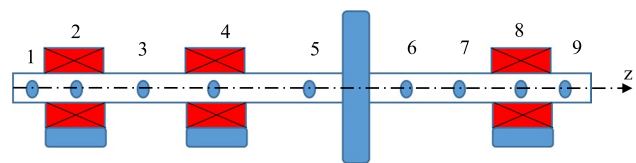

Fig. 1 FE model considered

$\{F_B\} = [F_u + F_x F_y]^T = \{F_u\} + \{F_b\}$ is the resultant force vector component. F_u is the unbalance force along with gravity force vector and F_b is the vector of roller bearing forces.

3 Methodology

3.1 Empirical mode decomposition (EMD)

Empirical mode decomposition is a nonlinear, non-stationary signal analysis technique that decomposes a signal into a series of full and nearly orthogonal intrinsic mode functions (IMFs). The IMF reflects oscillatory modes contained in the signal and functions as fundamental functions defined by the signal rather than predetermined kernels. A finite number of IMFs could be decomposed from the signal. The following definitions must be met by each IMF.

(1) The number of extreme and zero-crossings in the whole data set must be equal or deviate by no more than one.

(2) The mean value of the upper and lower envelopes is zero at any point.

The procedure for EMD and its algorithm is clearly explained in Fig. 2. The original signal is decomposed as follows after a series of computations.

$$x(t) = \sum_{i=0}^{n} c_i(t) + r_n(t) \qquad (2)$$

Fig.2 Flow diagram of EMD process
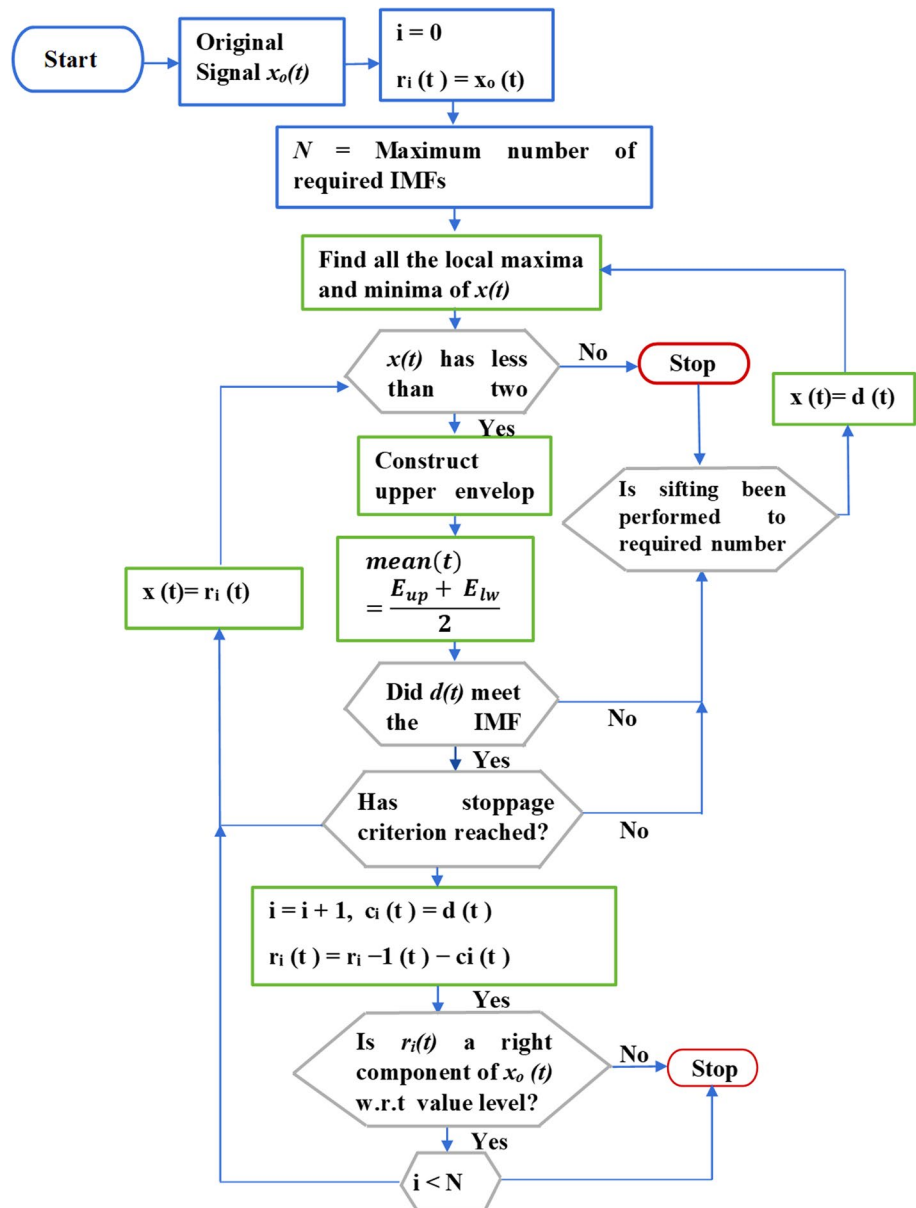
where $c_i(t)$ is the sum of IMF levels and $r_n(t)$ is the final residue.

EMD provides better diagnostic information about the system by analyzing its vibration response, sound, and acoustic emission signals than the conventional methods. IMFs use statistical characteristics to identify defects in machine elements' early stages.

3.2 Identification procedure via counter propagation neural network

Once the features are extracted, a machine learning approach can be conveniently adapted to identify the system parameters including faults. Several machine learning techniques such as support vector machines, neural networks, and neuro-fuzzy systems have been employed in this line. In the present work, the instar–outstar counter propagation neural network model is exploited. The concept of the Counter Propagation Neural Network (CPNN) was introduced by Robert Hecht-Nielsen[50]. This architecture is a novel combination of existing network types that provides versatility in using it. Figure 3 shows the network with inputs and outputs. The algorithm is provided with inputs in vector pairs as (x_1, y_1). CPNN learns to link an x vector on the input layer to a y vector on the output layer in this example. The CPNN will learn to approximate this mapping for every value of x in the range provided by the collection of training vectors if the connection between x and y can be represented by a continuous function, phi, such that $y = \Phi(x)$. Furthermore, if phi has an inverse, such that x is a function of y, the CPNN will learn the inverse mapping, $x = \Phi^{-1}(y)$. The first and second layers, that is, the input layer and Kohonen layer form an instar model, and the second and third layers, the Kohonen layer and output layer constitute an outstar model [51]. In this network, the second and third layers perform Kohonen and Grossberg learnings, respectively. Thus it combines unsupervised Kohonen learning and supervised Grossberg learning. The CPNN is much faster than BPNN, and there is no chance of its weights getting trapped in the local minima. However, it may be inferior to the BPNN in mapping applications.

3.3 Adaptive neuro-fuzzy inference system (ANFIS)

This section provides a brief description and capabilities of the Adaptive Neuro-Fuzzy Inference System (ANFIS). ANFIS systems use the capabilities of fuzzy logic and neural networks. Fuzzy logic maps the input data to desired output with highly connected neural network weighted processing elements. The parameters of fuzzy inference systems are tuned by neural network learning methods. With the application of neural networks, ANFIS refines the fuzzy IF–THEN rules. Different rules cannot share the same output membership function. The basic fuzzy inference system consists of fuzzy rules, data-driven membership functions, and fuzzy reasoning to derive the outputs. Out of many FIS systems, the Takagi–Sugeno Fuzzy system has many applications due to its linguistic interpretable capability.

The learning algorithm for ANFIS is a hybrid algorithm that is a combination of gradient descent and least-squares methods. A hybrid learning algorithm extracts rules from input–output data of the systems that are being modeled. The neural network of ANFIS fine-tunes the rules with updating weights of the rules. Many research articles have a greater explanation of ANFIS. Identification of an optimal fuzzy model concerning the training data reduces to a linear least-squares estimation problem. The method follows in two steps: (i) the First step involves the extraction of an initial fuzzy model from input–output data by using a cluster estimation method incorporating all possible input variables. (ii) In the next step the important input variables are identified by testing the significance of each variable in the initial fuzzy model. This initial fuzzy model can be selected based on the fuzzy rules framed by either using the subtractive
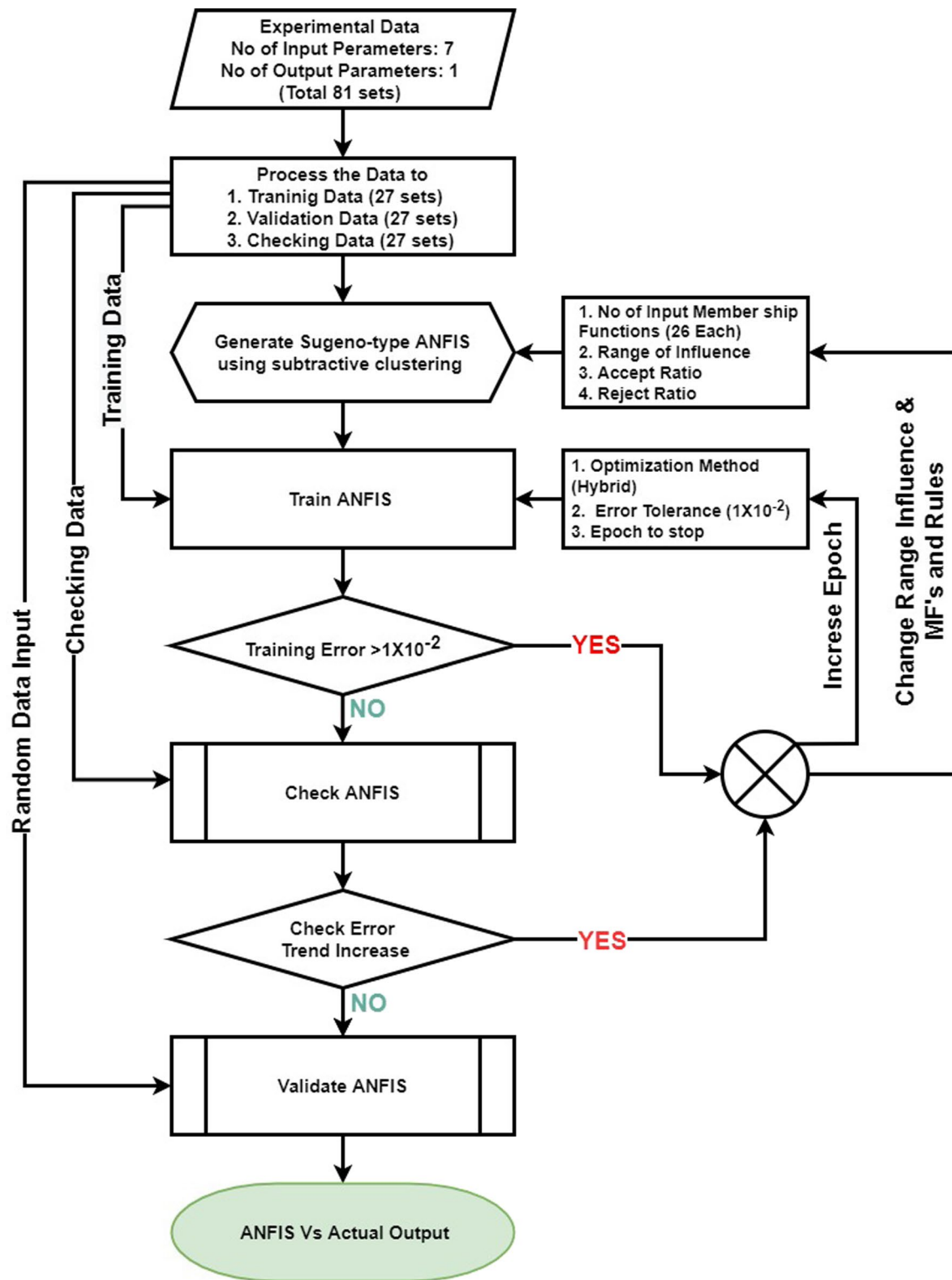
Fig. 3 Architecture of CPNN
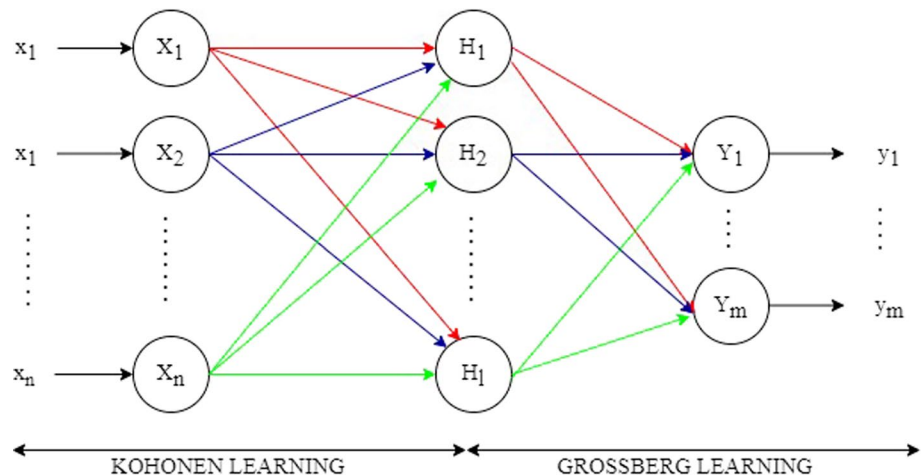
Fig. 4 Methodology of ANFIS for fault type identification
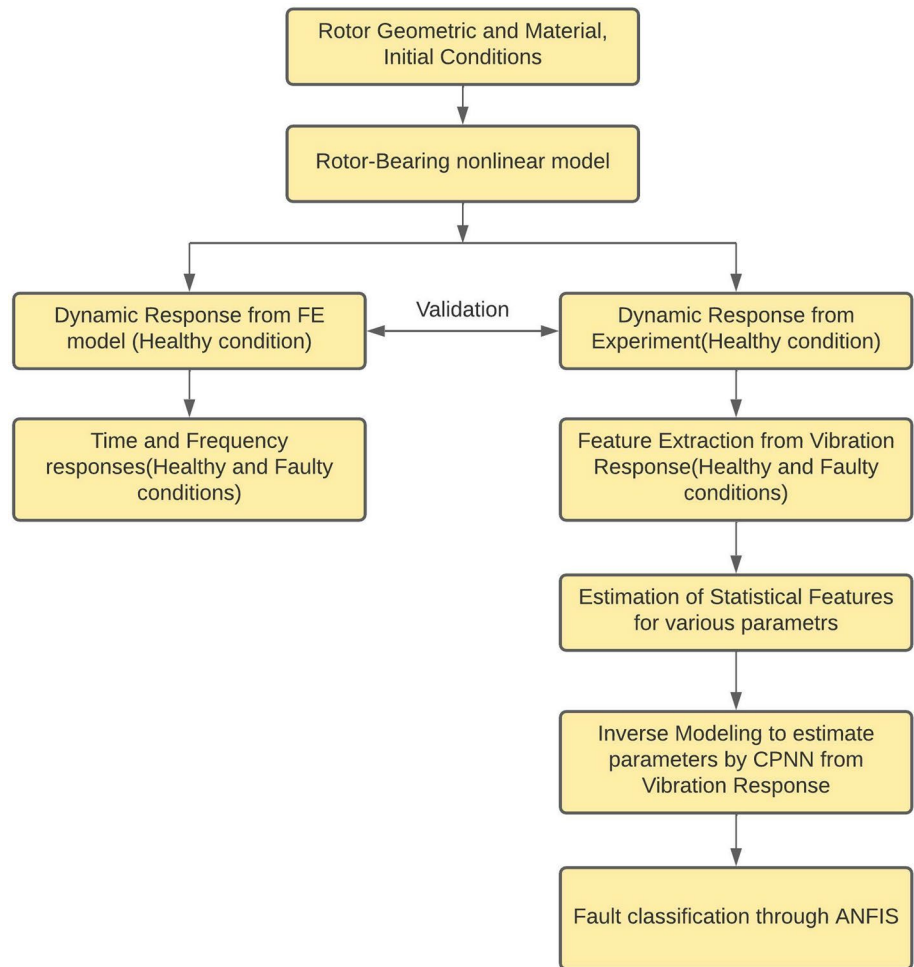
Fig. 5 Flowchart of diagnostic procedure

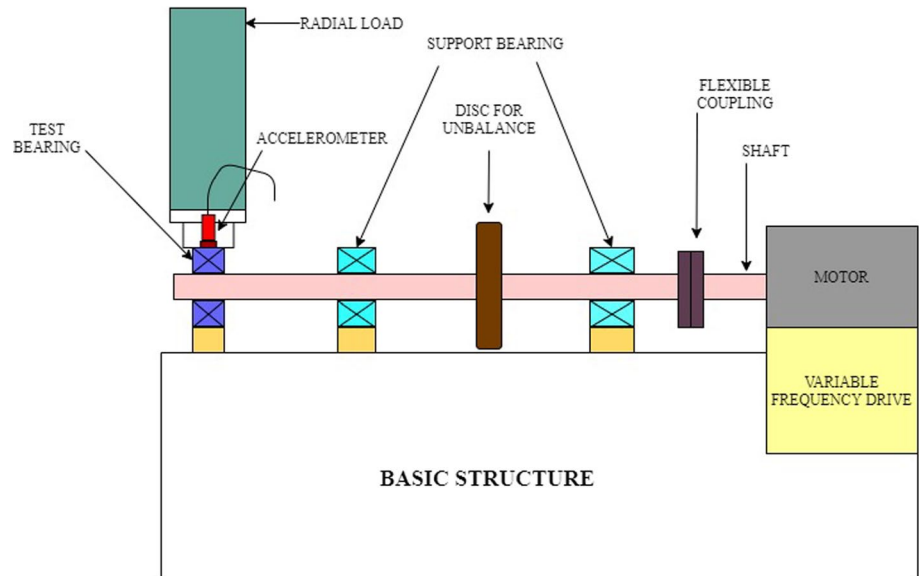**Fig. 6** Schematic diagram of an experimental setup

Table 1 Specification of the motor

Feature	Details
Phase	Single-phase induction motor
Rated power	1 HP, 0.75 kW
Pole	4
AC voltage	220–240 V
Speed	3000 rpm
Casing	Squirrel cage
Body	Cast iron

clustering technique or the grid partitioning method. In the current analysis, the subtractive clustering technique is used to identify the type of fault occurring in the rotor-bearing system. The cluster estimation technique helps in locating the cluster centers of the input–output data pairs. This in turn helps in the determination of the rules which are scattered in input–output space, as each cluster center is an indication of the presence of a rule.

3.4 Fault classification through ANFIS

The methodology for fault type identification by ANFIS is given in the below flow diagram. The experimental data collected from EMD and CPNN is divided into three data sets. The training data set is used for training the ANFIS, the Checking data set is used for checking the performance of ANFIS for variation in the data set and Validation data is used to find the outputs, i.e., type of fault from ANFIS. For fault type identification Sugeno type FIS with a subtractive clustering system is generated by providing input membership functions, Range of influence, and accept and reject ratios. The generated FIS is then trained with training data set. A training data set contains the first few columns as inputs and the last column as output (preidentified). A hybrid optimization method is used with an error tolerance is less than 1×10^{-2} and a max epoch of 100. If error tolerance is greater than 1×10^{-2} ANFIS needs to be re-trained with modifications in input membership functions, and range of influence for each input.

Once the training error is within the predefined error limit, ANFIS is checked for model data overfitting by training routine with checking data set. Generally, data overfit is identified by the trend of Root Mean Square Error (RMSE) curves. The model data overfit is identified by an increase in the error of checking data. If overfitting is observed then input parameters for the training of the ANFIS are altered, else ANFIS is validated with random input data. The percentage error in the output of ANFIS is calculated with the Actual output of random data. Figure 4 shows the flowchart for the fault classification through ANFIS.

Figure 5 shows the methodology of identification with feature extraction from signal and learning process using input–output training data. The computational FE model is developed to validate the response of the present experimental model in terms of frequency response at different speeds and different bearing fault conditions. This comparison is explained in Sect. 4.5. The statistical parameters were extracted from the raw response signals obtained from the experimental test rig in different operating conditions. Further, an inverse model is developed using CPNN and identified operating parameters from the vibration response. Later, ANFIS is used to classify the fault condition in the system.

Table 2 Specifications of the DPI testing bearing

Feature	Details
Bearing type	Roller (DPI N-304)
Number of rollers	10
Outside diameter	52 mm
Inside diameter	20 mm
Pitch diameter	36 mm
Roller diameter	07 mm
Weight	0.153 kg
Basic dynamic load rating	23.1 kN
Basic static load rating	19.2 kN
Limit speed	14,000 rpm
Material	High carbon chromium bearing steel of grade SAE J404

Fig. 7 Artificially generated defect on **a** roller bearing with 30% roller fault, **b** roller bearing with 60% inner race fault, and **c** roller bearing with 100% outer race fault
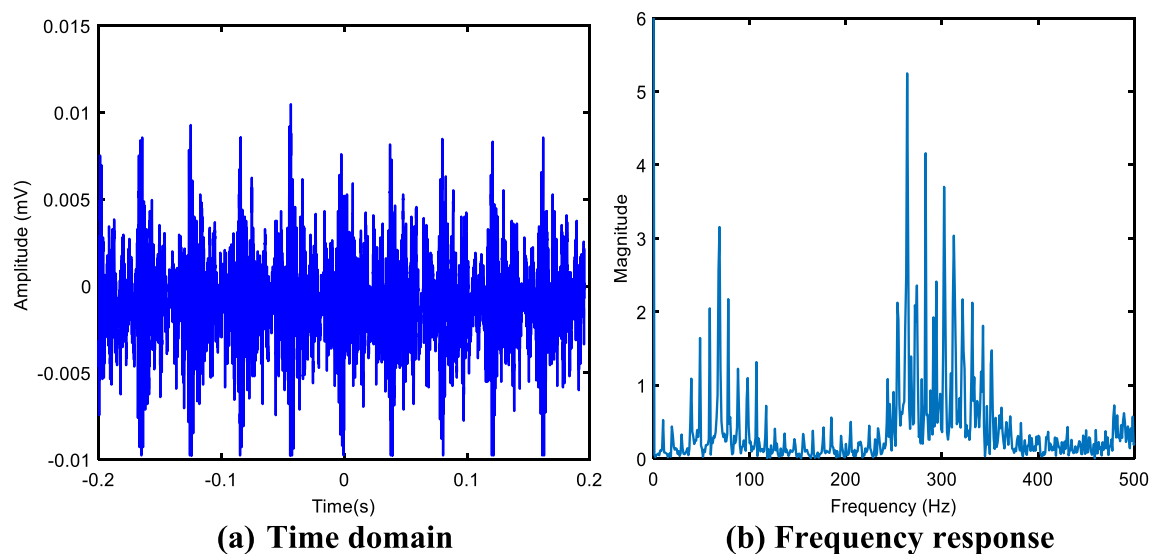

(a)   (b)   (c)

(a) Time domain　　　　**(b) Frequency response**
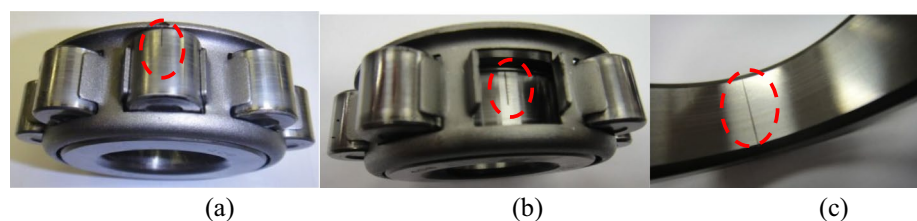
Fig. 8 Time and frequency response of the experimental test rig (100% of inner race fault): **a** time domain and **b** frequency response

4 Results and discussion

4.1 Construction of the experimental test rig and its components

The experimental test rig consists of a rotor-bearing system, driving unit, and hydraulic loading unit as shown in Fig. 6. The rig comprises a stainless steel shaft held between two single-row cylindrical roller bearings of SKFDPI N-304 type which are supported in bearing housings each at the end of the shaft. The single-phase motor is connected to the shaft with flexible coupling the specifications of the single-phase motor are depicted in Table 1. The speed of rotation using variable frequency drive from 500 to 3000 RPM can be achieved. A digital non-contact type tachometer is used to measure the rotational speed of the rotor. On the test bearing a radial load is applied with the help of the hydraulic loading arrangement. A data acquisition system is selected to monitor and acquire the vibration and acoustic signals. An OROS of 34 series, 4 channel, and 24-bit compact analyzer is employed in this research. It was employed to record the vibration signals at desired sampling rates. The hardware is comprised of 3 parts: (1) Piezoelectric accelerometer (2) Charge amplifier (3) Analyzer. An accelerometer was connected to the compact analyzer through a charge amplifier. The analyzer was further linked to a computer. The amplifier is very much essential to amplify the signals from an accelerometer that are generally weak. The amplifier also separates the sensor from the analyzer and display apparatus. A piezoelectric accelerometer with a sensitivity of 105 mV/g is positioned near the test bearing to capture vibration signals. This acceleration transducer takes measurements in

the zone of highest load, and the frequency-domain signal is presented when linked to a computer through a Fast Fourier Transform (FFT) analyzer. Because faults on the inner races or rolling components provide the greatest risk of exposure, the current experimental study includes these forms of defects as well. With the use of an Electrical Discharge Machine, faults are recreated by creating flaws on the races and rollers of the bearing. Thermal sensors are used to measure temperature change. The tests were carried out on artificially damaged bearings with the flaws depicted in Fig. 7. For ease of understanding let us consider Fault-1 is the surface fault on Bearing Roller, Fault-2 is the surface fault on the bearing inner race and Fault-3 is the surface fault on the bearing outer race. Different operating parameters such as radial load, temperature, and unbalanced phase angle are used as variables in addition to bearing faults, and response is recorded at various operating speeds of interest. The data is then familiarized with several fault situations that are reproduced at 500, 1500, and 2500 rpm. The vibration response was recorded at 500 Hz in all cases; with the frequency band, three to five kHz chosen for simplicity of spectra of bearing vibrations.

DPI N-304 roller testing bearing whose specifications are presented in Table 2.

Initially, the raw signals of the time domain and frequency response of the system from the experimental test rig are identified. Only in one case (100% of inner race fault) the raw signal of the time domain and frequency response of the system is shown in Fig. 8.
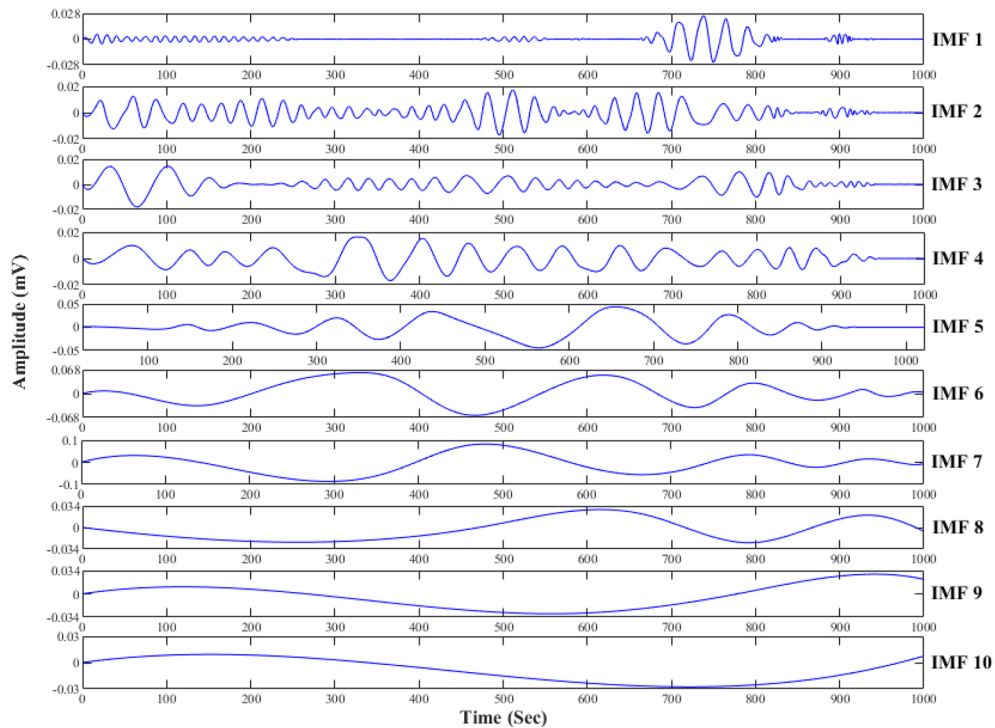
(a) Healthy bearing signal
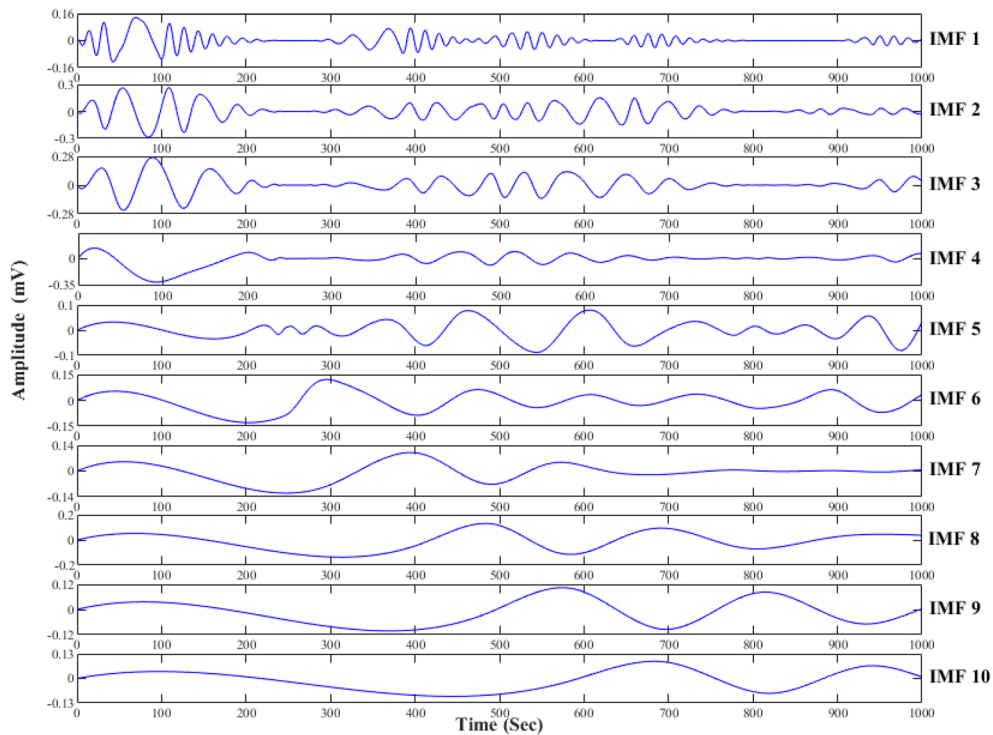
(b) Fault 1(Roller bearing with 30% roller fault)
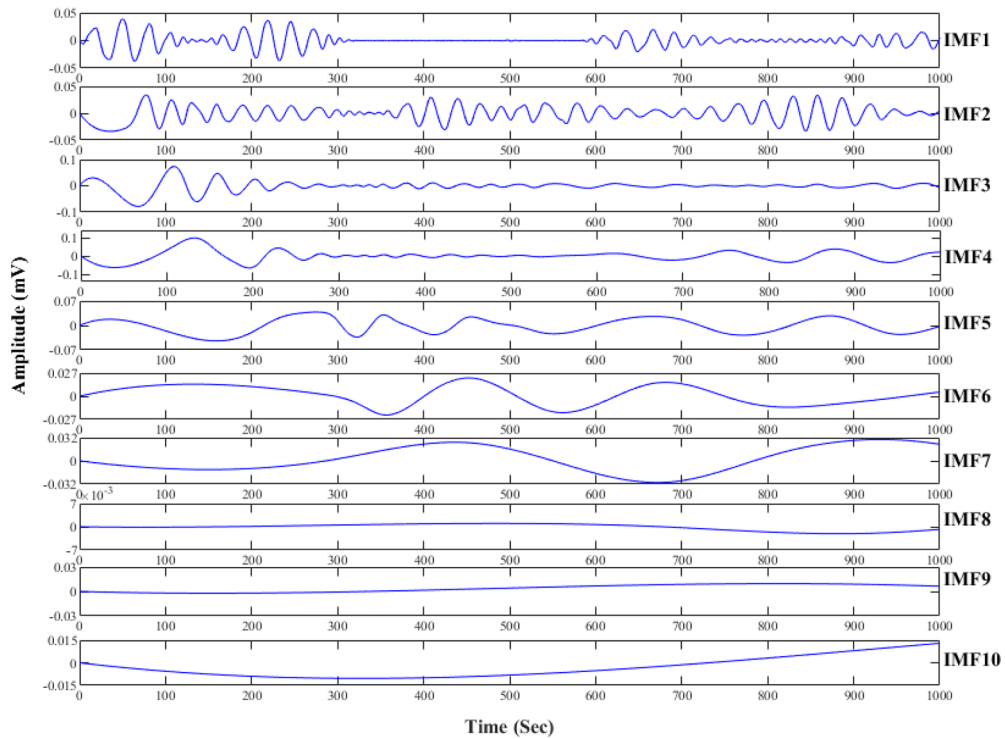
Fig. 9 The decomposed results of the vibration signals with EMD. **a** Healthy bearing signal, **b** Fault 1(roller bearing with 30% roller fault), **c** Fault 2 (roller bearing with 60% inner race fault), **d** Fault 3 (roller bearing with 100% outer race fault), **e** Fault 4 (roller bearing with 60% roller fault) and **f** Fault 5 (roller bearing with 100% inner race fault)
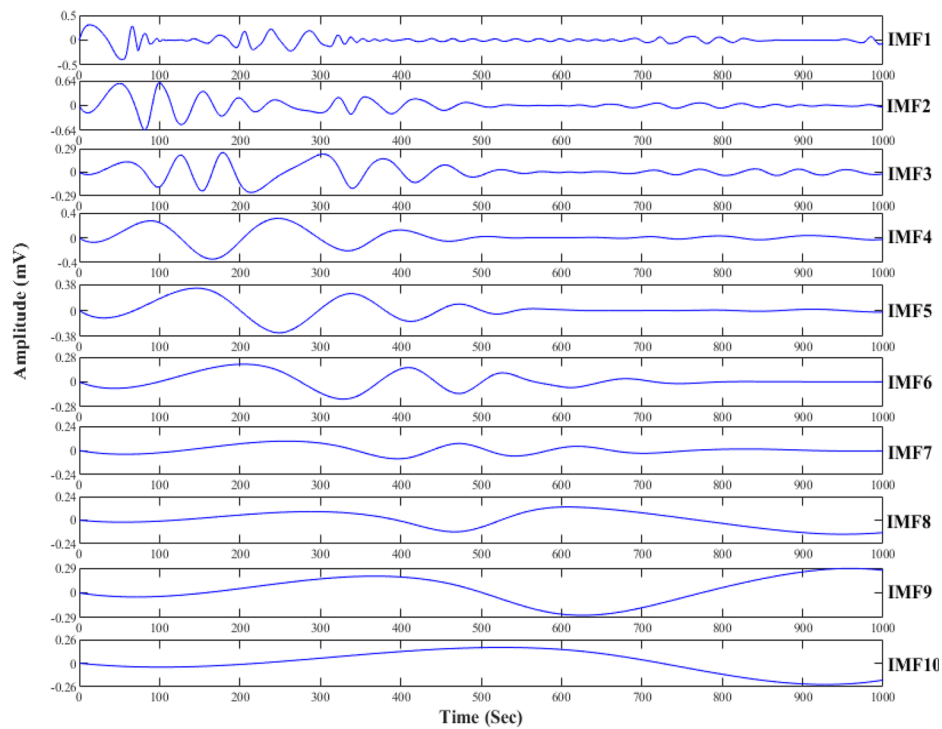
(c) Fault 2 (Roller bearing with 60% inner race fault)

(d) Fault 3 (Roller bearing with 100% outer race fault)

Fig. 9 (continued)

(e) Fault 4 (Roller bearing with 60% roller fault)

(f) Fault 5 (Roller bearing with 100% inner race fault)

Fig. 9 (continued)

Fig. 10 Frequency spectrum of IMFs for 0 to 500 Hz range. **a** No-fault (healthy bearing), **b** Fault 1(roller bearing with 30% roller fault), **c** Fault 2 (roller bearing with 60% inner race fault), **d** Fault 3(roller bearing with 100% outer race fault), **e** Fault 4 (roller bearing with 60% roller fault) and **f** Fault 5 (roller bearing with 100% inner race fault)
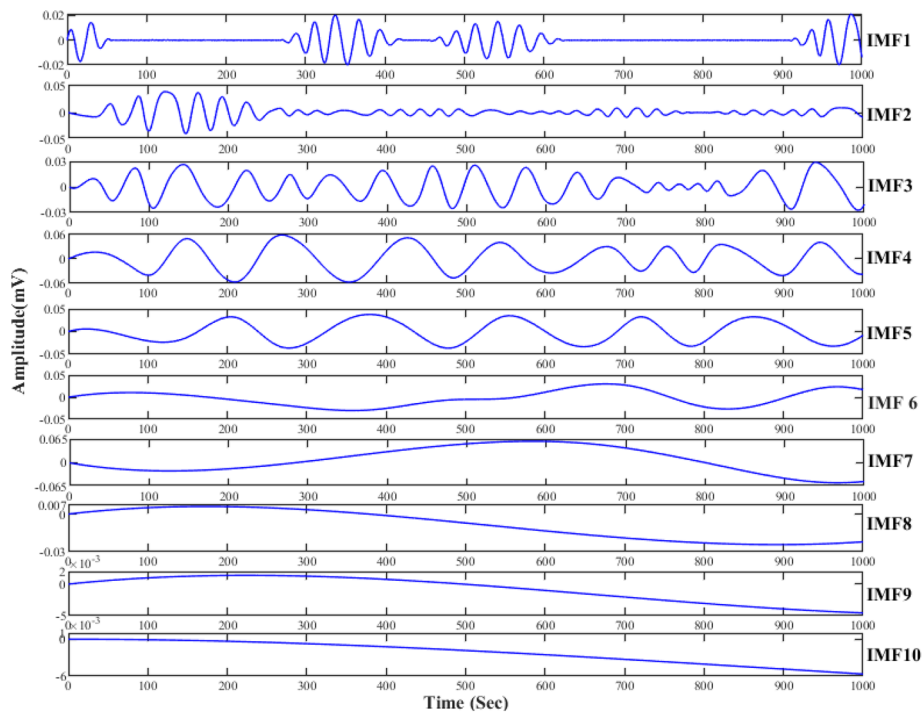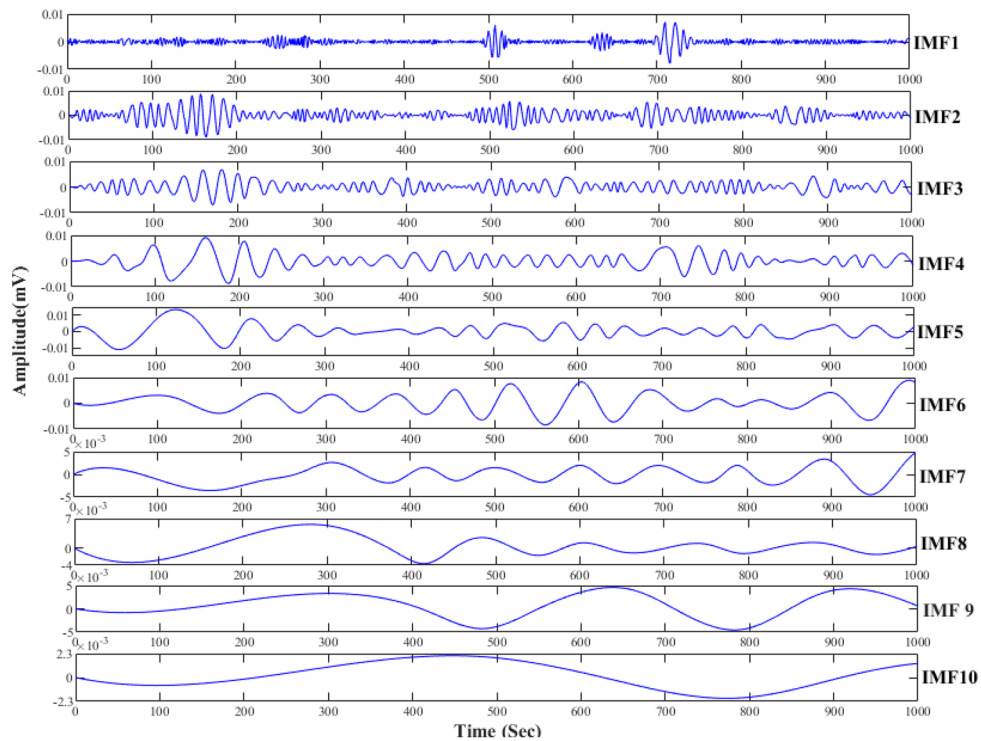

(a) No-fault (healthy bearing)

(b) Fault 1(Roller bearing with 30% roller fault)

(c) Fault 2 (Roller bearing with 60% inner race fault)

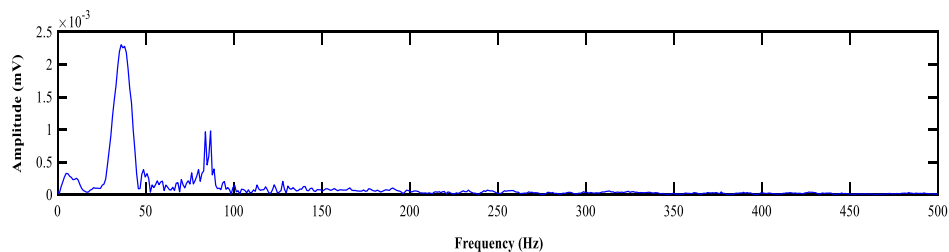(d) Fault 3(Roller bearing with 100% outer race fault)

(e)Fault 4 (Roller bearing with 60% roller fault)

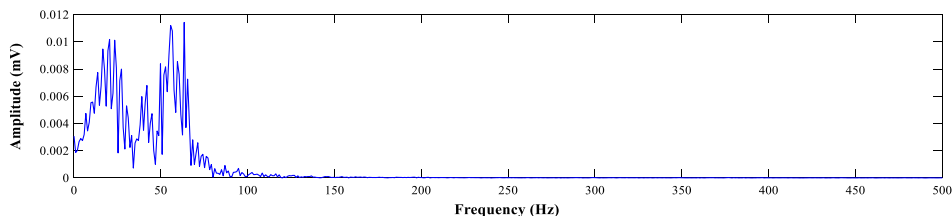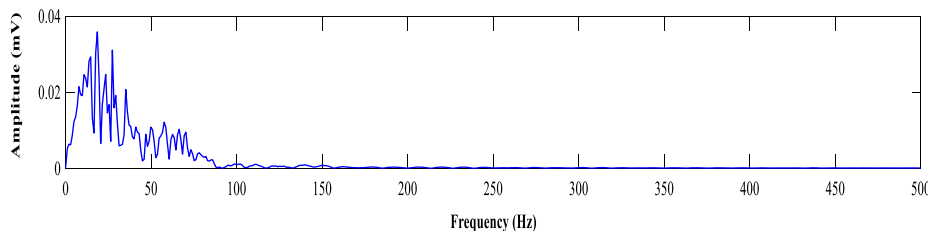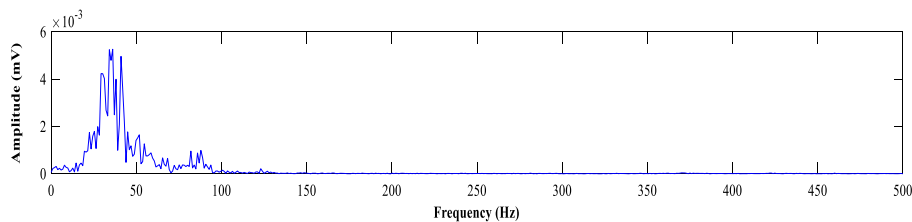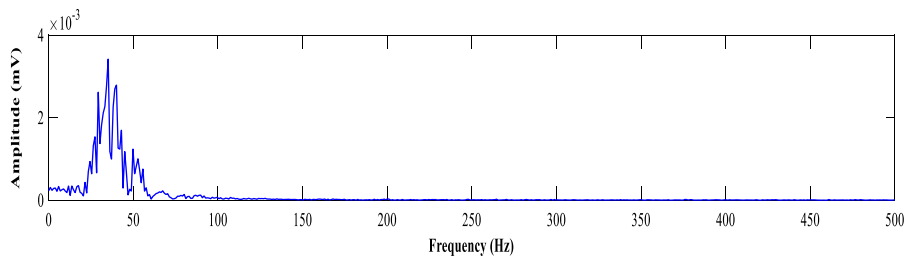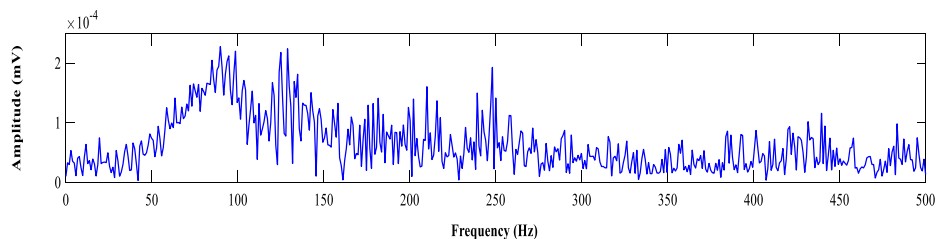(f) Fault 5 (Roller bearing with 100% inner race fault)

Table 3 Experimental data at a rotor speed of 500 rpm

Sl. no	Radial load (N)	Tempera-ture (°C)	Fault number	Unbalance phase angle	Mean	Kurtosis	Skewness	Peak to Peak	Variance	Standard deviation
1	500	28	1	0°	$1.09e^{-04}$	302.73	19.04	0.0801	− 320.178	3.78
2	500	34	2	90°	$1.20e^{-04}$	389.09	18.39	0.0436	− 200.714	4.41
3	500	42	3	180°	$1.40e^{-05}$	412.65	19.40	0.0328	− 1084.54	7.28
4	1000	28	2	180°	$8.18e^{-04}$	401.35	13.98	0.0142	227.0334	7.38
5	1000	34	3	0°	$1.74e^{-05}$	406.29	19.03	0.0354	− 85.0121	9.68
6	1000	42	1	90°	$1.32e^{-04}$	402.86	13.99	0.0175	− 72.7869	11.51
7	2000	28	3	90°	$1.20e^{-04}$	422.93	15.43	0.0834	− 20.0132	21.98
8	2000	34	1	180°	$1.43e^{-05}$	289.76	15.30	0.0384	− 1084.54	9.61
9	2000	42	2	0°	$3.02e^{-04}$	403.87	19.08	0.0212	− 85.0121	4.21
10	500	28	1	0°	$1.20e^{-05}$	260.62	19.87	0.0821	− 310.178	20.7
11	500	34	2	90°	$1.02e^{-05}$	476.87	21.98	0.0321	− 206.714	7.86
12	500	42	3	180°	$1.52e^{-04}$	273.63	22.42	0.0184	− 1093.54	8.63
13	1000	28	2	180°	$6.74e^{-04}$	438.27	14.09	0.0141	220.0334	7.72
14	1000	34	3	0°	$1.04e^{-05}$	506.01	22.08	0.0382	− 82.0121	6.43
15	1000	42	1	90°	$3.21e^{-04}$	409.88	19.76	0.0854	− 72.7869	3.9
16	2000	28	3	90°	$2.9e^{-04}$	238.74	19.88	0.0274	− 29.0132	4.86
17	2000	34	1	180°	$8.21e^{-04}$	287.09	19.19	0.0128	− 1099.54	5.92
18	2000	42	2	0°	$1.01e^{-04}$	226.93	16.87	0.0816	− 95.0121	11.97
19	500	28	1	0°	$1.84e^{-05}$	493.83	15.98	0.0301	− 324.178	22.09
20	500	34	2	90°	$8.66e^{-04}$	409.89	15.06	0.0384	− 203.714	22.76
21	500	42	3	180°	$4.8e^{-04}$	364.54	19.46	0.0863	− 1084.54	21.7
22	1000	28	2	180°	$2.0e^{-04}$	494.50	19.05	0.0147	227.0334	12.62
23	1000	34	3	0°	$4.33e^{-04}$	394.84	18.64	0.0384	− 85.0121	12.07
24	1000	42	1	90°	$4.09e^{-05}$	411.02	19.01	0.8976	− 72.7869	14.63
25	2000	28	3	90°	$2.40e^{-04}$	402.94	19.89	0.0249	− 20.0132	8.42
26	2000	34	1	180°	$1.45e^{-04}$	414.33	19.45	0.0148	− 1084.54	8.53
27	2000	42	2	0°	$1.70e^{-04}$	398.72	15.98	0.0784	− 85.0121	7.42

4.2 Time-domain analysis of the signal

Intrinsic mode functions for healthy and defective vibration signals are first obtained. Decomposition of time-domain signals for healthy and fault rotor-bearing systems are processed through the EMD algorithm and obtained ten intrinsic mode functions as shown in Fig. 9a–f.

It is observed that the faults in the inner race and on the roller are much inflecting the response of the system compared to a fault in the outer race. From these plots, it is very difficult to identify the type of fault and expertise required in analyzing this signal data. It is discussed earlier operating conditions can vary in addition to a fault in bearings. This makes the identification methods to be robust.

4.3 Frequency-domain analysis of signal

It is a well-known fact that the first parameter to predict any fault is by analyzing the frequency content of the signal. The time-domain signal shown in Fig. 8 and IMFs shown

in Fig. 9 as such does not provide any information about the fault. Further, Fig. 10a–f shows frequency response IMF1 for healthy and faulty condition bearings.

The primary peak frequency for a healthy bearing is 45 Hz, but numerous peaks emerge under various defective situations, and these peaks are caused by bearing defects. The bearing inner race and roller faults are much influencing the response of the system compared to outer race fault. As per the methodology, CPNN is used to extract the operating conditions from the time domain/IMF response statistical data. An inverse neural network model is developed to identify the different parameters such as radial load, temperature, fault number, and unbalanced phase angle from the known system response at different rotor speeds. Table 3 shows the experimental response data for various parameters. Training data consists of the signal characteristics namely statical parameters like mean, kurtosis, skewness, and peak to a peak value [52] as inputs, and corresponding operating parameters (radial load, temperature, fault type and unbalance phase angle) as outputs are employed a counter propagation neural

Table 4 Experimental data at a rotor speed of 1500 rpm

Sl. no	Radial Load (N)	Temperature (°C)	Fault number	Unbalance phase angle	Mean	Kurtosis	Skewness	Peak to Peak	Variance	Standard deviation
1	500	28	1	0°	$3.70e^{-03}$	333.03	22.848	0.1602	−416.231	4.914
2	500	34	2	90°	$2.00e^{-03}$	427.99	22.068	0.0872	−260.928	5.733
3	500	42	3	180°	$5.90e^{-04}$	453.95	23.28	0.0656	−1409.9	9.464
4	1000	28	2	180°	$9.76e^{-04}$	441.45	16.776	0.0284	295.1434	9.594
5	1000	34	3	0°	$7.08e^{-04}$	446.99	22.836	0.0708	−110.516	12.584
6	1000	42	1	90°	$2.46e^{-03}$	443.16	16.788	0.035	−94.623	14.963
7	2000	28	3	90^0	$5.36e^{-04}$	465.23	18.516	0.1668	−26.0172	28.574
8	2000	34	1	180°	$4.54e^{-04}$	318.76	18.36	0.0768	−1409.9	12.493
9	2000	42	2	0°	$2.35e{-03}$	444.27	22.896	0.0424	−110.516	5.473
10	500	28	1	0°	$2.98e^{-04}$	286.62	23.844	0.1642	−403.231	26.91
11	500	34	2	90°	$6.32e^{-04}$	524.57	26.376	0.0642	−268.728	10.218
12	500	42	3	180°	$6.82e^{-03}$	300.93	26.904	0.0368	−1421.6	11.219
13	1000	28	2	180°	$8.25e^{-04}$	482.07	16.908	0.0282	286.0434	10.036
14	1000	34	3	0°	$4.51e^{-04}$	556.61	26.496	0.0764	−106.616	8.359
15	1000	42	1	90°	$1.69e^{-03}$	450.88	23.712	0.1708	−94.623	5.07
16	2000	28	3	90°	$8.63\ e^{-03}$	262.64	23.856	0.0548	−37.7172	6.318
17	2000	34	1	180°	$1.45e^{-04}$	315.79	23.028	0.0256	−1429.4	7.696
18	2000	42	2	0°	$9.20e^{-03}$	249.63	20.244	0.1632	−123.516	15.561
19	500	28	1	0°	$0.94e^{-03}$	543.23	19.176	0.0602	−421.431	28.717
20	500	34	2	90°	$6.65e^{-03}$	450.89	18.072	0.0768	−264.828	29.588
21	500	42	3	180°	$5.24e^{-03}$	400.94	23.352	0.1726	−1409.9	28.21
22	1000	28	2	180°	$1.90e^{-03}$	543.9	22.86	0.0294	295.1434	16.406
23	1000	34	3	0°	$9.64e^{-03}$	434.34	22.368	0.0768	−110.516	15.691
24	1000	42	1	90°	$3.59e^{-04}$	452.12	22.812	1.7952	−94.623	19.019
25	2000	28	3	90°	$1.09e^{-03}$	443.24	23.868	0.0498	−26.0172	10.946
26	2000	34	1	180°	$8.84e^{-03}$	455.73	23.34	0.0296	−1409.9	11.089
27	2000	42	2	0°	$7.55e^{-03}$	438.52	19.176	0.1568	−110.516	9.646

network. A separate neural network identification model is used for different shaft speeds (Tables 4, 5).

Initially, training data consists of the central moments such as mean, kurtosis, skewness, and peak to peak as the inputs, and corresponding operating parameters are provided as outputs to train the network. After training the full CPNN with the instar–outstar learning rule, using adaptive learning rates, α, and β, the weights of hidden and output layers are obtained for an error tolerance of 1e−4. Here learning rate $\alpha = 0.4$ and momentum factor $\beta = 0.01$ is employed throughout. Figure 11 shows the convergence trend with different hidden nodes to estimate the correct number of hidden nodes at a rotor speed of 500 rpm. The mean square error is low and converges at a faster rate when the number of hidden nodes is equal to five.

Further, to show the capabilities of CPNN over BPNN a comparison was made for the convergence trend at three rotor speeds (500 rpm, 1500 rpm, and 2500 rpm) with five

hidden nodes shown in Figs. 12, 13, and 14, respectively. BPNN is a common method and is reliable in the identification of random data analysis. Initially, training data consists of the central moments such as mean, kurtosis, skewness, and peak to peak as the inputs, and corresponding operating parameters are provided as outputs to train the network. The parameters such as learning rate of 0.6, momentum rate of 0.9, and activation function are sigmoid. The parameters are verified for the error tolerance of 1e−4.

It is observed that in all three cases the CPNN is converging faster with less RMSE compared to BPNN. This reduces the computational time for the designers and helps in predicting accurate data. Table 6 depicts the test data, which includes three scenarios in which the targets are provided. The neural network's projected outcomes are compared to the measured values. In all three situations, the difference between anticipated and actual parameter values is less than three percent.

Table 5 Experimental data at a rotor speed of 2500 rpm

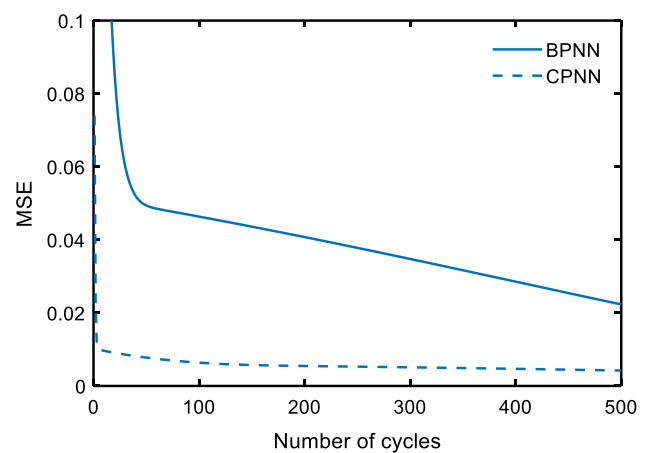| Sl. no	Radial Load (N)	Temperature (°C)	Fault number	Unbalance phase angle	Mean	Kurtosis	Skewness	Peak to peak	Variance	Standard deviation
1	500	28	1	0°	$3.29e^{-04}$	544.94	34.272	0.20025	−457.855	5.40
2	500	34	2	90°	$3.64e^{-03}$	700.32	33.102	0.109	−287.021	6.30
3	500	42	3	180°	$4.26e^{-04}$	742.7	34.92	0.082	−1550.89	10.41
4	1000	28	2	180°	$2.46e^{-03}$	722.4	25.164	0.0355	324.6578	10.55
5	1000	34	3	0°	$5.20e^{-05}$	731.32	34.254	0.0885	−121.567	13.84
6	1000	42	1	90°	$3.98e^{-04}$	725.18	25.182	0.04375	−104.085	16.45
7	2000	28	3	90°	$3.69e^{-04}$	761.24	27.774	0.2085	−28.6189	31.43
8	2000	34	1	180°	$4.30e^{-04}$	521.58	27.54	0.096	−1550.89	13.74
9	2000	42	2	0°	$9.07e^{-04}$	726.96	34.344	0.053	−121.567	6.02
10	500	28	1	0°	$3.61e^{-04}$	469.16	35.766	0.20525	−443.555	29.60
11	500	34	2	90°	$3.08e^{-04}$	858.36	39.564	0.08025	−295.601	11.23
12	500	42	3	180°	$4.58e^{-04}$	492.54	40.356	0.046	−1563.76	12.34
13	1000	28	2	180°	$2.02e^{-03}$	788.86	25.362	0.03525	314.6478	11.03
14	1000	34	3	0°	$3.13e^{-04}$	910.88	39.744	0.0955	−117.277	9.19
15	1000	42	1	90°	$9.65e^{-04}$	737.74	35.568	0.2135	−104.085	5.57
16	2000	28	3	90°	$8.95e^{-04}$	429.72	35.784	0.0685	−41.4889	6.94
17	2000	34	1	180°	$2.47e^{-03}$	516.72	34.542	0.032	−1572.34	8.46
18	2000	42	2	0°	$3.04e^{-04}$	408.44	30.366	0.204	−135.867	17.11
19	500	28	1	0°	$5.53e^{-04}$	888.84	28.764	0.07525	−463.575	31.5887
20	500	34	2	90°	$2.60e^{-03}$	737.82	27.108	0.096	−291.311	32.54
21	500	42	3	180°	$1.46e^{-03}$	656.12	35.028	0.21575	−1550.89	31.03
22	1000	28	2	180°	$6.28e^{-03}$	890.1	34.29	0.03675	324.6578	18.04
23	1000	34	3	0°	$1.30e^{-03}$	710.72	33.552	0.096	−121.567	17.26
24	1000	42	1	90°	$1.23e^{-04}$	739.86	34.218	2.244	−104.085	20.92
25	2000	28	3	90°	$7.21e^{-03}$	725.22	35.802	0.06225	−28.6189	12.04
26	2000	34	1	180°	$4.37e^{-04}$	745.74	35.01	0.037	−1550.89	12.19
27	2000	42	2	0°	$5.132e^{-03}$	717.66	28.764	0.196	−121.567	10.61
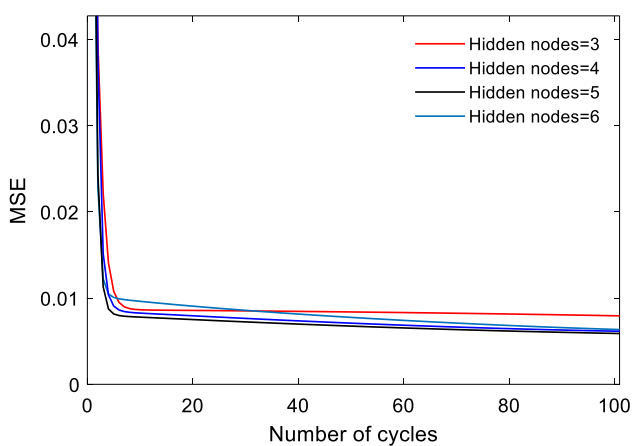
Fig. 11 Convergence trend

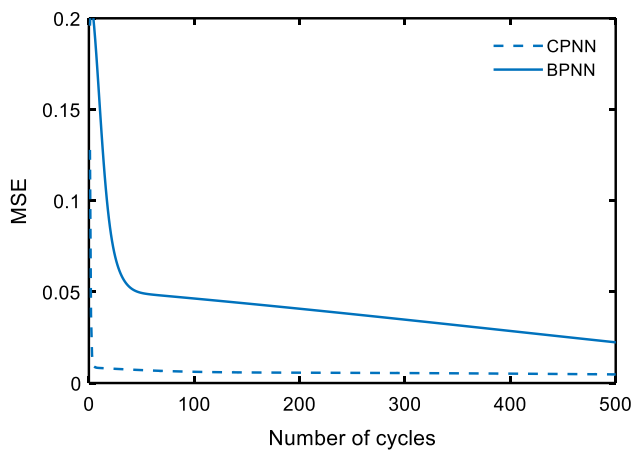**Fig. 12** Convergence trend (speed 500 rpm)

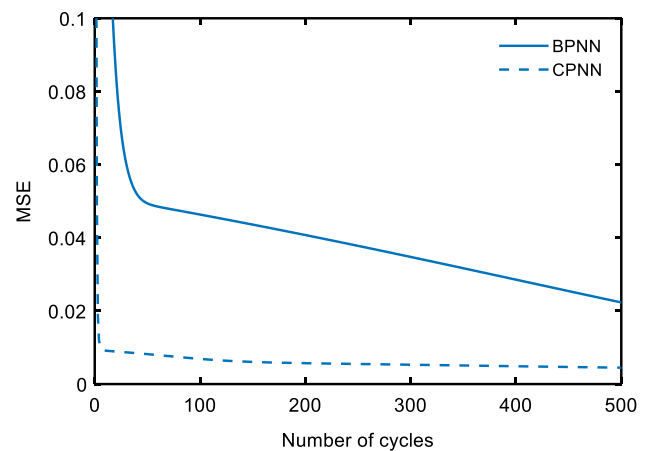**Fig. 13** Convergence trend (speed 1500 rpm)

Fig. 14 Convergence trend (speed 2500 rpm)

Table 6 Identified results

Sl. no	Speed (rpm)	Mean×10⁻⁴	Kurtosis	Skewness	Peak to peak	Radial Load (N)		Temperature (°C)		Fault number		Unbalance phase angle		% Error
						Predicted	Actual	Predicted	Actual	Predicted	Actual	Predicted	Actual	
1	500	8.662	302.97	19.04	0.0809	500	499	28	27.5	1	1	0°	0°	1.78
2	1500	1.096	387.03	18.39	0.0436	1000	1001	34	33	2	2	90°	90°	2.9
3	2500	2.412	411.76	19.40	0.0328	2000	1998	42	43	3	3	180°	180°	2.32

Table 7 ANFIS parameters

Parameter	Value	Remarks
Type of FIS	Takagi−Surgeon type	
Number of input	7	
Number of outputs	1/1	
Input MF type	Gbellmf	Bell Curve
Output type	Linear	(first-order Takagi−Surgeon type)
Number of fuzzy rules	27	
Learning algorithm	Hybrid	
Number of nodes	442	
Number of epochs	100	
Error tolerance	1×10^{-2}	
Actual RMS error	0.000591281 at 100 epoch	Fault type
Evaluation method	Training and checking data versus ANFIS output	Both the data are considered to get accurate results

4.4 Fault identification by ANFIS

In the current work, the ANFIS methodology is described in the flow diagram shown in Fig. 4. MATLAB R2018b software is used for ANFIS simulations. Operating parameters like radial Load, bearing temperature, and unbalance phase angle are collected from CPNN output; statistical parameters of IMF like mean, kurtosis, skewness, and peak-to-peak variation are collected from EMD for different faults and speeds of the rotor-bearing system are provided as inputs and fault type is provided as output to ANFIS. A total of 81 samples are collected from experimental simulations of know faults.
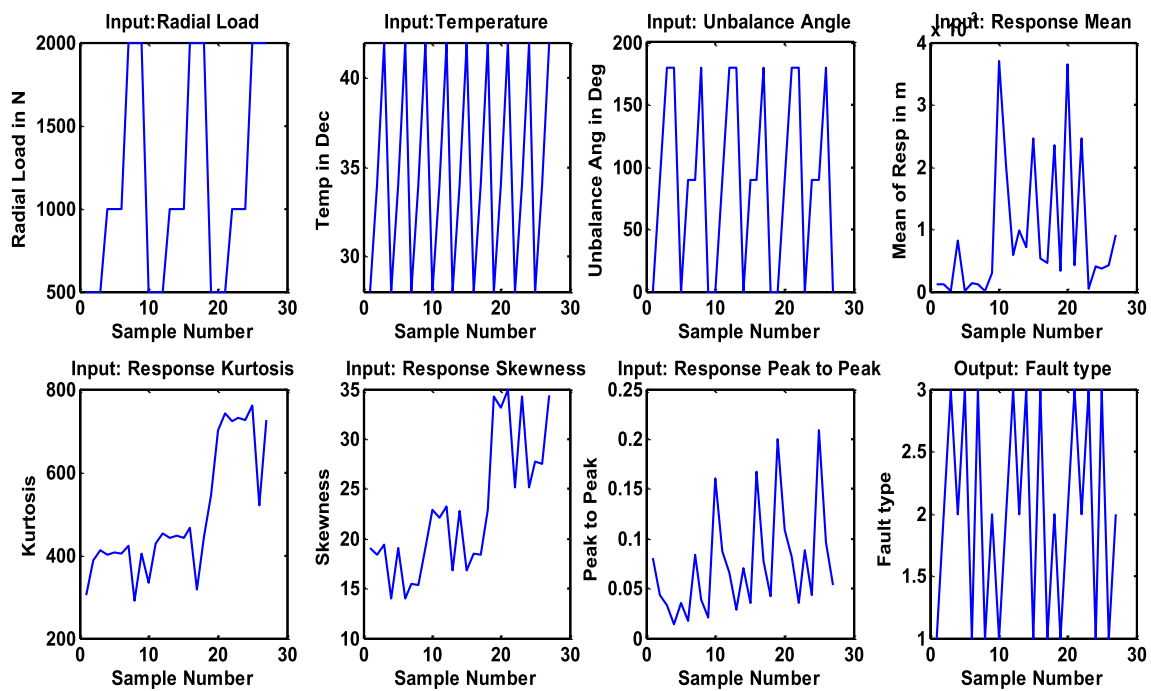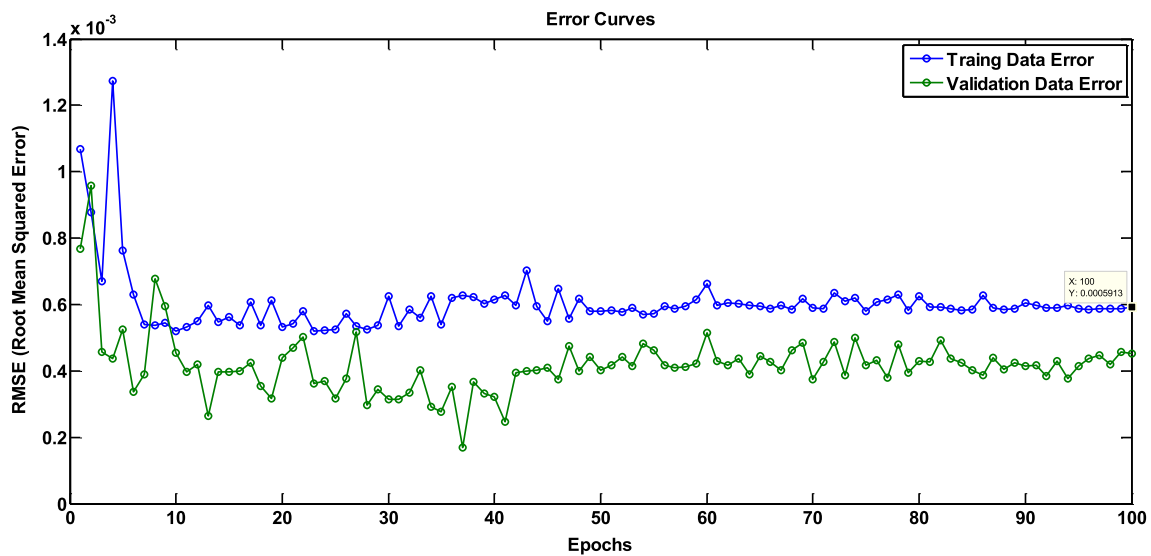
Fig. 15 Training data set inputs and output

Fig. 16 Training error versus validation error

Out of 81 samples, that were used for training, 27 samples were used for checking and 27 were used for testing. 40 samples are collected randomly for validation of ANFIS (only input provided to ANFIS) for identification of fault type. Genfis2 surgeon type ANFIS generates FIS structure from data using subtractive clustering. The number of the input membership function is 26 for each input, which generates 27 fuzzy if–then rules, connected by T-norm (Fuzzy AND) operators. A hybrid learning algorithm is used in training ANFIS. The training of ANFIS is done by minimal error
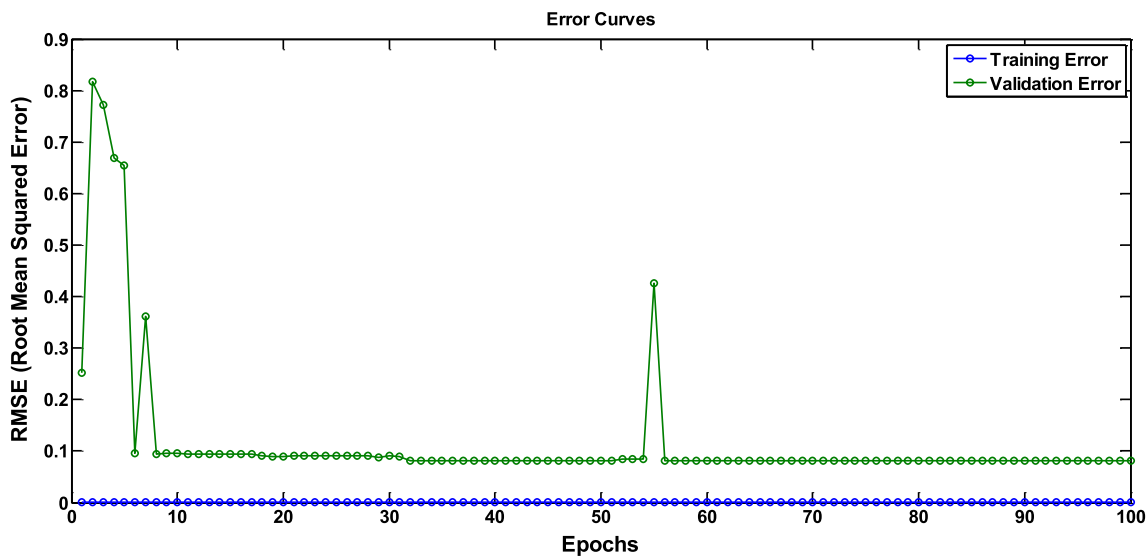
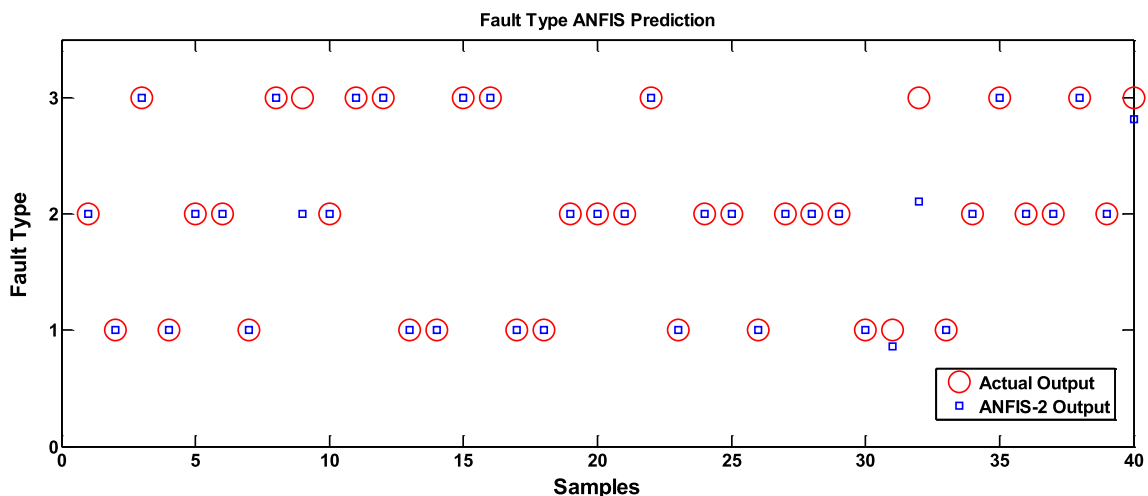**Fig. 17** ANFIS model overfitting curves (training and checking data)

Fig. 18 ANFIS OUTPUT prediction

tolerance with a designated epoch number. The training process stops whenever the designated epoch number is reached or the training error goal is achieved. In the current case, we considered 1×10^{-2} errors with 100 epochs. The Trained ANFIS system can be evaluated with any other input data. The results of outputs from ANFIS are compared with checking and validated data. Table 7 shows the parameters used for ANFIS simulation. Figure 15 shows the data collected for training.

The data for training is collected randomly from the experimental results. All the 7 input and their know outputs are shown in the figure. From the figure, it is clear that the collected data is very random and is not structured. Similar data is collected for checking, validation, and random data to identify the capabilities of ANFIS for fault type.

The Generated ANFIS is trained with training and validation data. The Error for the 100 epoch is shown in Fig. 16. The Trend of both the error curves is decreasing

Table 8 Error in prediction of fault type by ANFIS

S. No.	Exp output	ANFIS output	Error
1	2	1.99	0.01
2	1	1.00	0.00
3	3	2.99	0.01
4	1	1	0.00
5	2	2.0	0.00
6	2	1.72	0.28
7	1	0.99	0.01
8	3	2.99	0.01
9	3	2.88	0.12
10	2	1.99	0.01
11	3	2.99	0.01
12	3	2.99	0.01
13	1	0.99	0.01
14	1	1.00	0.00
15	3	3.00	0.00
16	3	3.01	0.01
17	1	0.99	0.01
18	1	0.99	0.01
19	2	2.00	0.00
20	2	2.00	0.00
21	2	0.01	1.99
22	3	3.00	0.00
23	1	1.00	0.00
24	2	1.79	0.21
25	2	2.09	0.09
26	1	0.99	0.01
27	2	2.03	0.03
28	2	1.93	0.064
29	2	2.00	0.00
30	1	1.00	0.00
31	1	0.99	0.01
32	3	3.00	0.00
33	1	1.00	0.00
34	2	2.00	0.00
35	3	2.70	0.29
36	2	1.99	0.01
37	2	2.00	0.00
38	3	3.00	0.00
39	2	1.99	0.01
40	3	2.99	0.01

trend with a training error of 0.0005913 and a validation error of 0.0004508. With these outputs, it can be concluded that the error is minimal than the target and

show a better result even with limited data of 81 samples. Figure 17 shows the error curves for training and checking data.

To identify the model overfitting of the ANFIS system, the ANFIS system is trained with training and checking data sets as input arguments. At close to the 55th epoch the checking data error shows an abnormal peak. This could be due to the number of data used for training being smaller than the number of modifiable parameters. The error before and after this peak is close by and maintains the same trend. So considering the model parameters before or after the peak does not have much variation. From the plot, it can be interpreted that the trained ANFIS system does not possess model over or data overfitting. As the results of error curves are promising, ANFIS is used to validate with random data. Forty samples of random experimental data are collected and only input parameters are provided with trained ANFIS to identify the fault type. Figure 18 shows the output comparison of ANFIS with experimental output for all three types of faults. Table 8 presents the error from the experimental output or actual output. The Error values are rounded off to the second digit. An error less than 0.05 is considered as matching output, an error between 0.05 to 0.1 is considered an alarming output, and an error above 0.1 is considered as strongly not matching or caution outputs. Out of 40 random sample inputs, only one prediction is strongly not matching with experimental or actual output. The Trained ANFIS is 100% accurate in predicting Fault type-1 (12 samples out of 12 are matching), 87.5% in predicting Fault type-2 (14 samples out of 16 are matching, one sample is strongly not matching), and 96% in predicting Fault type-3 (10 samples out of 12 are matching, two are close by).

A mathematical model to simulate bearing fault is developed using finite element methods. Using EMD raw time series data from both finite element models and experiments are decomposed to their intrinsic functions. EMD natural processes the statistical features from the time series data. In this article, statistical features such as mean, kurtosis, skewness, peak to peak, variance, and standard deviation are employed in fault identification. Further, these statistical data are used in CPNN and ANFIS schemes for the effective detection of faults.

There are some limitations also presented in the above study while conducting the experiments the temperature change, misalignments, and rotor–stator rubbing. Selection and decision of statistical parameters used to train the neural network and number of trained data sets.
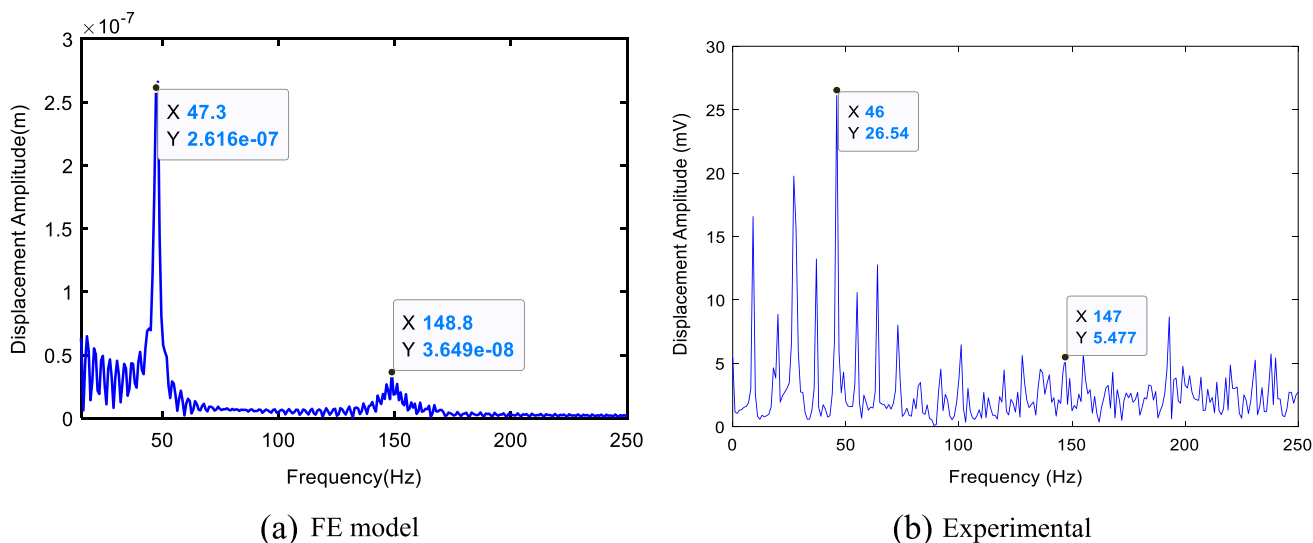
(a) FE model

(b) Experimental

Fig. 19 Frequency response at a rotor speed of 2500 rpm. **a** FE model and **b** experimental

(a) Rotor speed 500 rpm
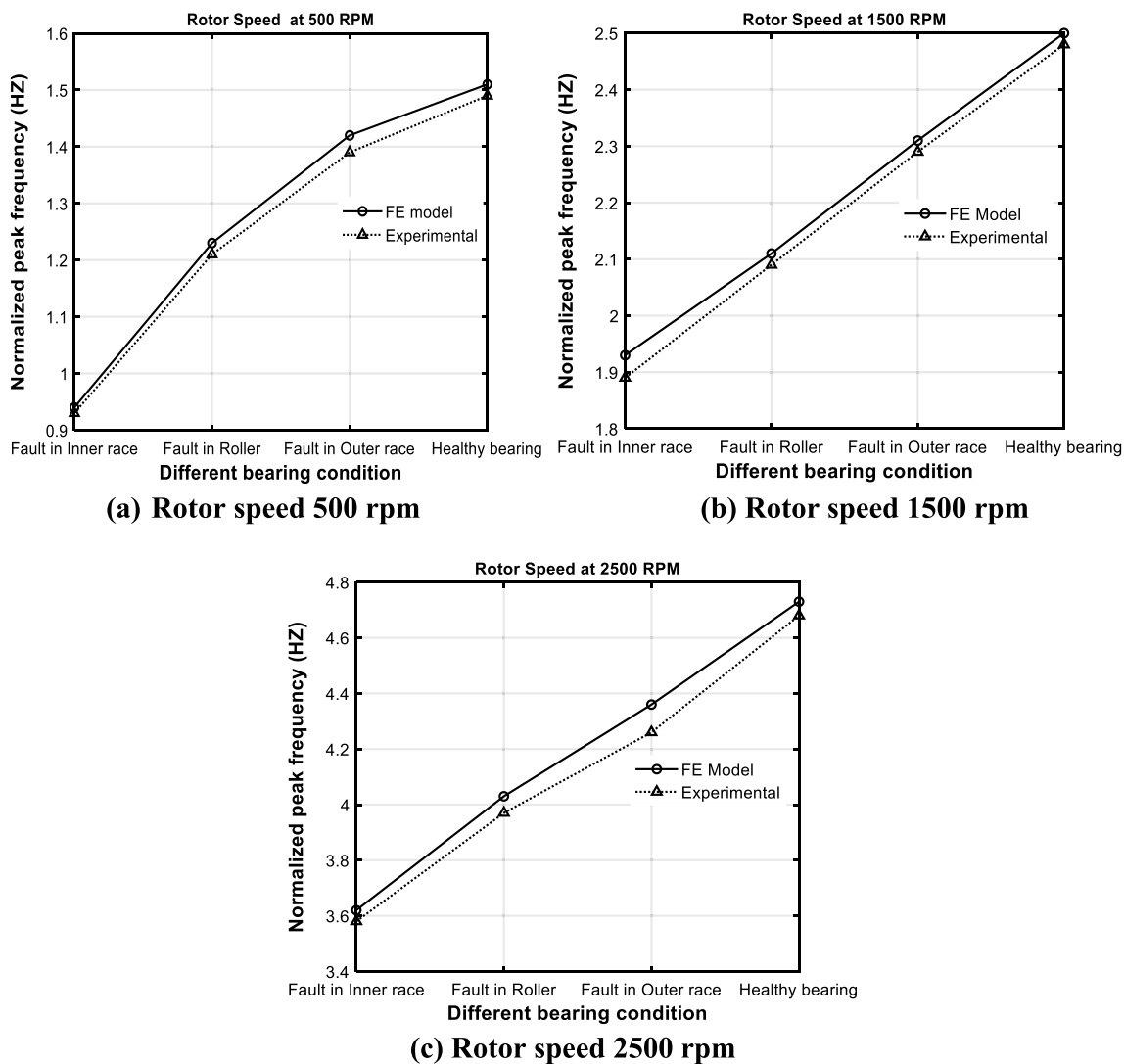
(b) Rotor speed 1500 rpm

(c) Rotor speed 2500 rpm

Fig. 20 Comparison of FE and experimental model. **a** Rotor speed 500 rpm, **b** rotor speed 1500 rpm, and **c** rotor speed 2500 rpm
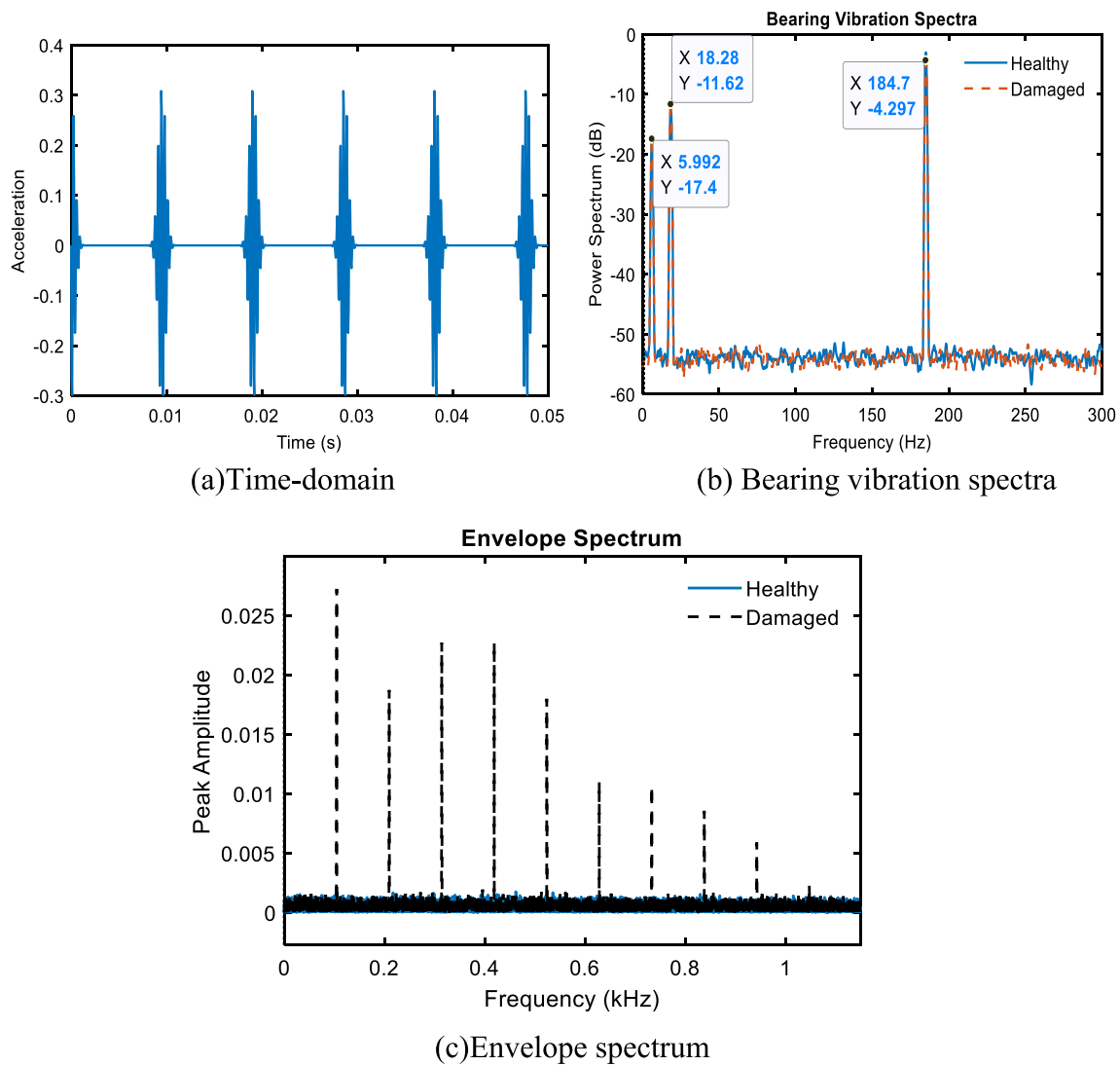
(a)Time-domain

(b) Bearing vibration spectra

(c)Envelope spectrum

Fig. 21 Time and frequency response at bearing node with inner race fault. **a** Time domain, **b** bearing vibration spectra, and **c** envelope spectrum

4.5 Validation

For the healthy bearing condition at a rotor speed of 2500 rpm, a comparison of the frequency response from the finite element (FE) model and the experimental model is performed. The frequency response from FE and the experimental model is shown in Fig. 19.

The first dominating peak frequency from FE and experimental are 47.3 Hz and 46 Hz, respectively. The values are compared in terms of frequency these frequency values are reasonably coming close. The comparison of the dominant peak frequency for the healthy and different bearing fault conditions from the FE model and Experimental at various speeds are shown in Fig. 20.

It is observed that the identified dominant peak frequencies from FE and experimental are closer.

Further, with the finite element model, the time and frequency response with different bearing faults are identified. An interactive MATLAB code is developed to identify these responses. At a constant rotor speed of 15,000 rpm and a bearing inner defect, Fig. 21 illustrates the time and frequency response at the bearing location.

It is observed from the bearing vibration spectra, that for the faulty condition the initial two dominant peak frequencies are 5.99 Hz and 18.28 Hz. whereas the speed-dependent
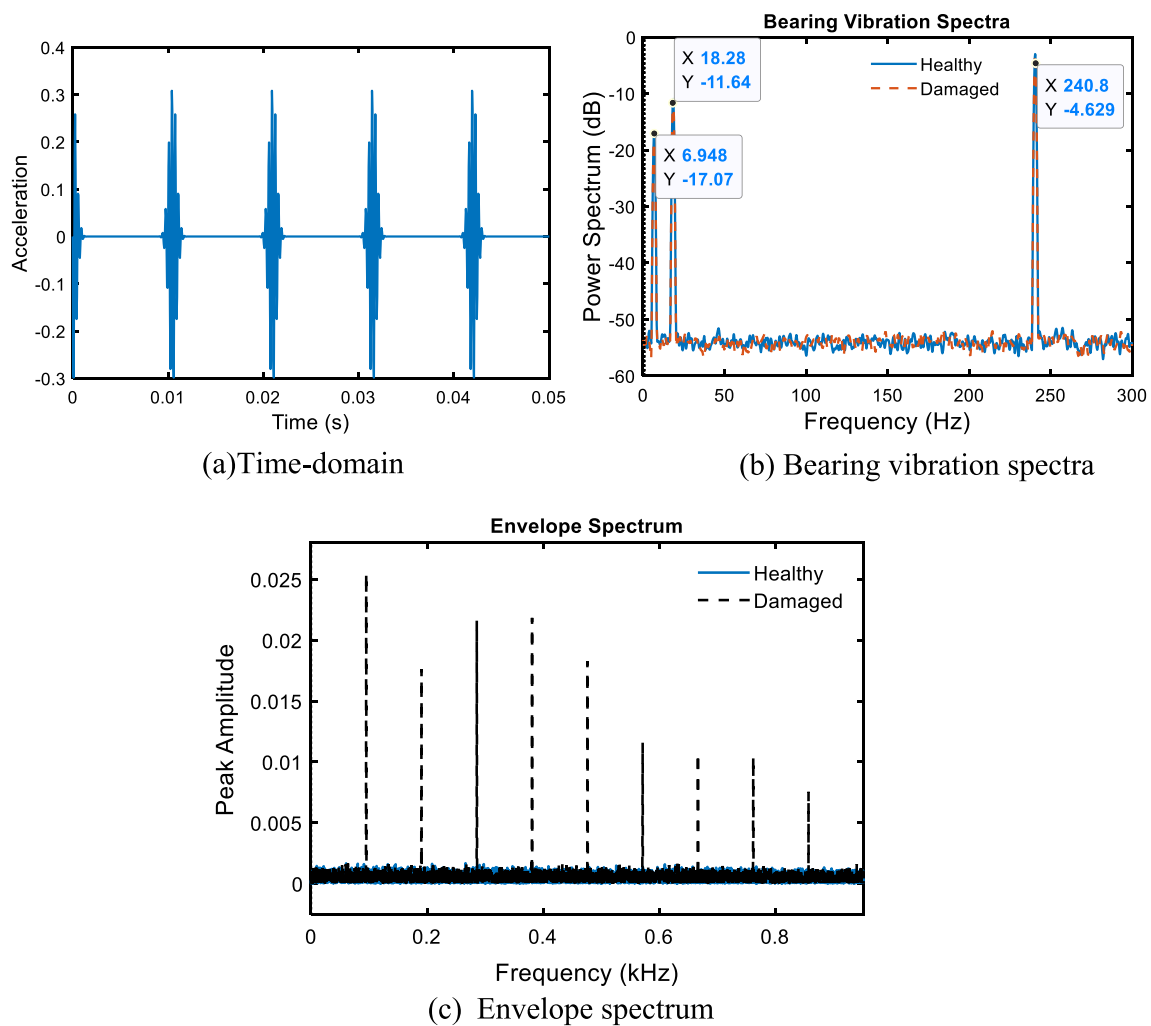
(a) Time-domain

(b) Bearing vibration spectra

(c) Envelope spectrum

Fig. 22 Time and frequency response at bearing node with roller fault. **a** Time domain, **b** bearing vibration spectra, and **c** envelope spectrum

peak frequency is 184.7 Hz. It is seen in the amplitude difference for the healthy and damaged conditions from the envelope spectrum. Figure 22 depicts the time and frequency response at a bearing location with a roller defect at a constant rotor speed of 15,000 rpm.

It is observed from the bearing vibration spectra, that for the faulty condition the initial two dominant peak frequencies are 6.94 Hz and 18.28 Hz. whereas the speed-dependent peak frequency is 240.8 Hz. Compare to the inner race faulty condition the first and third dominant peak frequencies are increased slightly. It is seen in the amplitude difference for the healthy and damaged conditions from the envelope spectrum. Figure 23 shows the time and frequency response at

bearing location at a constant rotor speed of 15,000 rpm with outer race fault.

It is observed from the bearing vibration spectra, that for the faulty condition the initial two dominant peak frequencies are 8.59 Hz and 22.31 Hz. whereas the speed-dependent peak frequency is 265.9 Hz. Compare to inner race and roller faulty condition the dominant peak frequencies are increasing. It indicates the faults on the inner race and roller are much influencing the response of the system compared to the outer race fault. It is seen in the amplitude difference for the healthy and damaged conditions from the envelope spectrum.
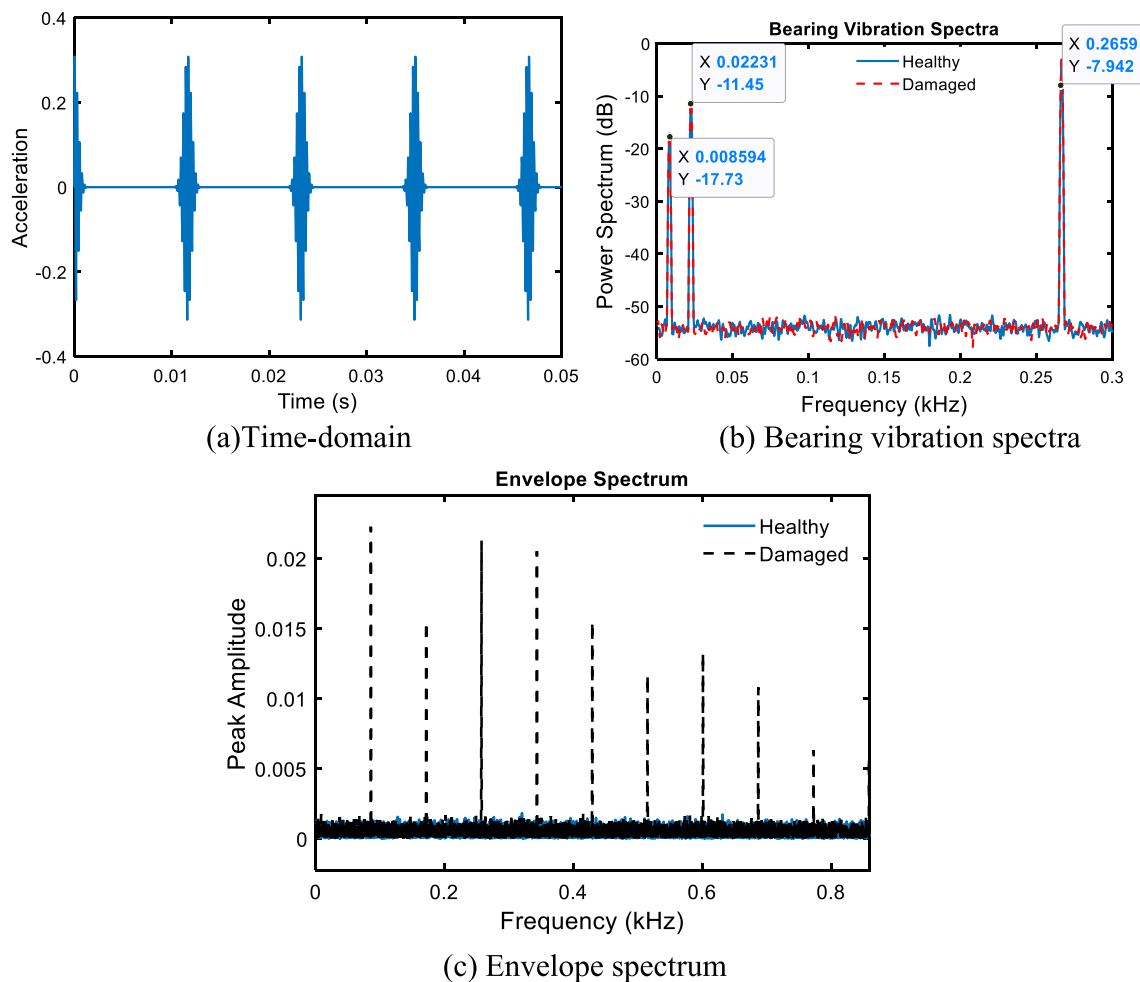
(a) Time-domain

(b) Bearing vibration spectra

(c) Envelope spectrum

Fig. 23 Time and frequency response at bearing node with outer race fault. **a** Time domain, **b** bearing vibration spectra, and **c** envelope spectrum

5 Conclusions

This research paper proposed a methodology for parameter and fault type identification from vibration response through empirical mode decomposition (EMD), counter propagation neural network (CPNN), and adaptive neuro-fuzzy inference system (ANFIS). Initially, an experimental rotor-bearing model was established to study the dynamics of the system under different operating conditions. The experimental results are validated with FEM simulation results for a healthy rotor-bearing system. Both time-domain and frequency-domain results are compared and found that the results are with minimal deviation. For the healthy and defective circumstances, the empirical mode decomposition approach was utilized to break down the extracted signal into intrinsic mode functions. CPNN was used to predict the operating parameters and ANFIS Classifies and predicts the faults in roller bearing of rotor systems. The following were the concluding remarks of the present work:

- It was observed from Intrinsic Mode Functions (IMF) that the faults on the inner race and the roller are much more influencing the response of the system compared to the fault on the outer race.
- It was observed from frequency-domain analysis of IMF that the dominant peak frequency for the healthy bearing was 45 Hz, whereas for various faulty conditions the multiple peaks forming these peaks are due to bearing faults.
- It was observed that the first dominant peak frequency in a healthy system from the finite element model and experimental are 47.3 Hz and 46 Hz. The values are compared in terms of frequency these frequency values are reasonably coming close.
- CPNN with five hidden layer neurons perfectly generalize the input–output relationship in extraction or prediction of operating conditions.
- CPNN was superior and faster compared to BPNN for feature prediction and extraction.

- It was observed that the trained ANFIS is 100% accurate in predicting Fault type-1 87.5% in predicting Fault type-2 and 96% in predicting Fault type-3.
- From the FE model also the inference from the frequency response was identified that the faults on the inner race and the roller were much influencing the response of the system compared to faults on the outer race.
- The amplitude change also clearly demonstrates the faulty conditions.

Declarations

References

1. Wang WJ, Chen J, Wu XK, Wu ZT (2001) The application of some non-linear methods in rotating machinery fault diagnosis. Mech Syst Signal Process 15:697–705. https://doi.org/10.1006/mssp.2000.1316

2. Samanta B, Al-Balushi KR, Al-Araimi SA (2006) Artificial neural networks and genetic algorithm for bearing fault detection. Soft Comput 10:264–271. https://doi.org/10.1007/s00500-005-0481-0

3. Samanta B, Al-Balushi KR, Al-Araimi SA (2004) Bearing fault detection using artificial neural networks and genetic algorithm. EURASIP J Adv Signal Process 2004:1–12. https://doi.org/10.1155/S1110865704310085

4. Janjarasjitt S, Ocak H, Loparo KA (2008) Bearing condition diagnosis and prognosis using applied nonlinear dynamical analysis of machine vibration signal. J Sound Vib 317:112–126. https://doi.org/10.1016/j.jsv.2008.02.051

5. Feng K, Jiang Z, He W, Qin Q (2011) Rolling element bearing fault detection based on optimal antisymmetric real Laplace wavelet. Measurement 44:1582–1591. https://doi.org/10.1016/j.measurement.2011.06.011

6. Volpi SL, Lazzerini B, Stefanescu D (2009) Time evolution analysis of bearing faults. ACTA

7. Bianchini C, Immovilli F, Cocconcelli M et al (2011) Fault detection of linear bearings in brushless AC linear motors by vibration analysis. IEEE Trans Ind Electron 58:1684–1694. https://doi.org/10.1109/TIE.2010.2098354

8. Tandon N, Choudhury A (1999) A review of vibration and acoustic measurement methods for the detection of defects in rolling element bearings. Tribol Int 32:469–480. https://doi.org/10.1016/S0301-679X(99)00077-8

9. Cococcioni M, Lazzerini B, Volpi SL (2013) Robust diagnosis of rolling element bearings based on classification techniques. IEEE Trans Ind Inform 9:2256–2263. https://doi.org/10.1109/TII.2012.2231084

10. Hou S, Li Y, Wang Z (2010) A resonance demodulation method based on harmonic wavelet transform for rolling bearing fault diagnosis. Struct Health Monit 9:297–308. https://doi.org/10.1177/1475921709352144

11. Tang L, Liu X, Wu X et al (2021) Defect localization on rolling element bearing stationary outer race with acoustic emission technology. Appl Acoust 182:108207. https://doi.org/10.1016/j.apacoust.2021.108207

12. Mączak J, Jasiński M (2018) Model-based detection of local defects in gears. Arch Appl Mech 88:215–231. https://doi.org/10.1007/s00419-017-1321-2

13. Inturi V, Sabareesh GR, Penumakala PK (2020) Bearing fault severity analysis on a multi-stage gearbox subjected to fluctuating speeds. Exp Tech 44:541–552. https://doi.org/10.1007/s40799-020-00370-z

14. Patil S, Jalan AK, Marathe AM (2022) Support vector machine for misalignment fault classification under different loading conditions using vibro-acoustic sensor data fusion. Exp Tech. https://doi.org/10.1007/s40799-021-00533-6

15. Parey A, El Badaoui M, Guillet F, Tandon N (2006) Dynamic modelling of spur gear pair and application of empirical mode decomposition-based statistical analysis for early detection of localized tooth defect. J Sound Vib 294:547–561. https://doi.org/10.1016/j.jsv.2005.11.021

16. Li H, Yin Y (2012) Bearing fault diagnosis based on Laplace wavelet transform. Indones J Electr Eng Comput Sci 10:2139–2150

17. Han T, Chao Z (2021) Fault diagnosis of rolling bearing with uneven data distribution based on continuous wavelet transform and deep convolution generated adversarial network. J Braz Soc Mech Sci Eng 43:425. https://doi.org/10.1007/s40430-021-03152-9

18. Mcfadden PD, Cook JG, Forster LM (1999) Decomposition of gear vibration signals by the generalised S transform. Mech Syst Signal Process 13:691–707. https://doi.org/10.1006/mssp.1999.1233

19. Jha RK, Swami PD (2022) Failure prognosis of rolling bearings using maximum variance wavelet subband selection and support vector regression. J Braz Soc Mech Sci Eng 44:49. https://doi.org/10.1007/s40430-021-03345-2

20. Tabrizi A, Garibaldi L, Fasana A, Marchesiello S (2015) Early damage detection of roller bearings using wavelet packet decomposition, ensemble empirical mode decomposition and support vector machine. Meccanica 50:865–874. https://doi.org/10.1007/s11012-014-9968-z

21. Lin J, Qu L (2000) Feature extraction based on Morlet wavelet and its application for mechanical fault diagnosis. J Sound Vib 234:135–148. https://doi.org/10.1006/jsvi.2000.2864

22. Walczak B, Massart DL (1997) Noise suppression and signal compression using the wavelet packet transform. Chemom Intell Lab Syst 36:81–94. https://doi.org/10.1016/S0169-7439(96)00077-9

23. Tikkanen PE (1999) Nonlinear wavelet and wavelet packet denoising of electrocardiogram signal. Biol Cybern 80:259–267. https://doi.org/10.1007/s004220050523

24. Learned RE, Willsky AS (1995) A wavelet packet approach to transient signal classification. Appl Comput Harmon Anal 2:265–278. https://doi.org/10.1006/acha.1995.1019

25. Chao JZ, Chen J, Guo X (2012) Gear fault diagnosis method based on ensemble empirical mode decomposition energy entropy and support vector machine. J Cent South Univ (Sci Technol) 43:932–939

26. Georgoulas G, Loutas T, Stylios CD, Kostopoulos V (2013) Bearing fault detection based on hybrid ensemble detector and empirical mode decomposition. Mech Syst Signal Process 41:510–525. https://doi.org/10.1016/j.ymssp.2013.02.020

27. Li C, Valente de Oliveira J, Cerrada M et al (2016) Observer-biased bearing condition monitoring: from fault detection to multi-fault classification. Eng Appl Artif Intell 50:287–301. https://doi.org/10.1016/j.engappai.2016.01.038

28. Lei Y, He Z, Zi Y (2009) Application of an intelligent classification method to mechanical fault diagnosis. Expert Syst Appl 36:9941–9948. https://doi.org/10.1016/j.eswa.2009.01.065

29. Chen Z, Deng S, Chen X et al (2017) Deep neural networks-based rolling bearing fault diagnosis. Microelectron Reliab 75:327–333. https://doi.org/10.1016/j.microrel.2017.03.006

30. Jia F, Lei Y, Lin J et al (2016) Deep neural networks: a promising tool for fault characteristic mining and intelligent diagnosis of rotating machinery with massive data. Mech Syst Signal Process 72–73:303–315. https://doi.org/10.1016/j.ymssp.2015.10.025

31. Han T, Tian Z, Yin Z, Tan ACC (2020) Bearing fault identification based on convolutional neural network by different input modes. J Braz Soc Mech Sci Eng 42:474. https://doi.org/10.1007/s40430-020-02561-6

32. Mutra RR, Srinivas J, Rządkowski R (2021) An optimal parameter identification approach in foil bearing supported high-speed turbocharger rotor system. Arch Appl Mech 91:1557–1575. https://doi.org/10.1007/s00419-020-01840-x

33. Mutra RR, Srinivas J (2021) Parametric design of turbocharger rotor system under exhaust emission loads via surrogate model. J Braz Soc Mech Sci Eng 43:117. https://doi.org/10.1007/s40430-021-02809-9

34. McFadden PD, Smith JD (1984) Vibration monitoring of rolling element bearings by the high-frequency resonance technique—a review. Tribol Int 17:3–10. https://doi.org/10.1016/0301-679X(84)90076-8

35. Zhou F, Xu P, Lin K (2021) Early warning analysis of online vibration fault characteristics of motor base screw loosening based on similarity measurement theory. Arch Appl Mech 91:1219–1231. https://doi.org/10.1007/s00419-020-01820-1

36. Cai J, Xiao Y, Fu L (2021) Fault diagnosis of rolling bearing based on fractional Fourier instantaneous spectrum. Exp Tech. https://doi.org/10.1007/s40799-021-00478-w

37. Moshrefzadeh A, Fasana A (2017) Planetary gearbox with localised bearings and gears faults: simulation and time/frequency analysis. Meccanica 52:3759–3779. https://doi.org/10.1007/s11012-017-0680-7

38. Ho D, Randall RB (2000) Optimisation of bearing diagnostic techniques using simulated and actual bearing fault signals. Mech Syst Signal Process 14:763–788. https://doi.org/10.1006/mssp.2000.1304

39. Rai VK, Mohanty AR (2007) Bearing fault diagnosis using FFT of intrinsic mode functions in Hilbert-Huang transform. Mech Syst Signal Process 21:2607–2615. https://doi.org/10.1016/j.ymssp.2006.12.004

40. Mutra RR, Srinivas J (2022) An optimization-based identification study of cylindrical floating ring journal bearing system in automotive turbochargers. Meccanica 57:1193–1211. https://doi.org/10.1007/s11012-022-01507-7

41. Ben Ali J, Fnaiech N, Saidi L et al (2015) Application of empirical mode decomposition and artificial neural network for automatic bearing fault diagnosis based on vibration signals. Appl Acoust 89:16–27. https://doi.org/10.1016/j.apacoust.2014.08.016

42. Geng Z, Zhang Y, Li C et al (2020) Energy optimization and prediction modeling of petrochemical industries: an improved convolutional neural network based on cross-feature. Energy 194:116851. https://doi.org/10.1016/j.energy.2019.116851

43. Bui D-K, Nguyen TN, Ngo TD, Nguyen-Xuan H (2020) An artificial neural network (ANN) expert system enhanced with the electromagnetism-based firefly algorithm (EFA) for predicting the energy consumption in buildings. Energy 190:116370. https://doi.org/10.1016/j.energy.2019.116370

44. Joshi AV (2020) Perceptron and Neural Networks. In: Joshi AV (ed) Machine learning and artificial intelligence. Springer International Publishing, Cham, pp 43–51

45. Chen H, Miao F, Chen Y et al (2021) A hyperspectral image classification method using multifeature vectors and optimized KELM. IEEE J Sel Top Appl Earth Obs Remote Sens 14:2781–2795. https://doi.org/10.1109/JSTARS.2021.3059451

46. Zhao H, Liu J, Chen H et al (2022) Intelligent diagnosis using continuous wavelet transform and gauss convolutional deep belief network. IEEE Trans Reliab. https://doi.org/10.1109/TR.2022.3180273

47. Wu D, Wu C (2022) Research on the time-dependent split delivery green vehicle routing problem for fresh agricultural products with multiple time windows. Agriculture 12:793. https://doi.org/10.3390/agriculture12060793

48. Zhou X, Ma H, Gu J et al (2022) Parameter adaptation-based ant colony optimization with dynamic hybrid mechanism. Eng Appl Artif Intell 114:105139. https://doi.org/10.1016/j.engappai.2022.105139

49. Yao R, Guo C, Deng W, Zhao H (2022) A novel mathematical morphology spectrum entropy based on scale-adaptive techniques. ISA Trans 126:691–702. https://doi.org/10.1016/j.isatra.2021.07.017

50. Hecht-Nielsen R (1987) Counterpropagation networks. Appl Opt, AO 26:4979–4984

51. Chen B-H, Huang S-C, Yen J-Y (2018) Counter-propagation artificial neural network-based motion detection algorithm for static-camera surveillance scenarios. Neurocomputing 273:481–493. https://doi.org/10.1016/j.neucom.2017.08.002

52. Mohanty A (2015) Machinery Condition Monitoring: Principles and Practices. In: Routledge & CRC, NY. https://www.routledge.com